1996ApJ...460.1042A

THE ASTROPHYSICAL JOURNAL, 460:1042–1063, 1996 April 1

OBSERVATIONS OF SOLAR CARBON MONOXIDE WITH AN IMAGING INFRARED SPECTROGRAPH. I. THERMAL BIFURCATION REVISITED

THOMAS R. AYRES[1]
Center for Astrophysics and Space Astronomy, University of Colorado, Campus Box 389, Boulder, CO 80309;
ayres@vulcan.colorado.edu

AND

DOUGLAS RABIN
National Solar Observatory, National Optical Astronomy Observatories, P.O. Box 26732, Tucson, AZ 85726; drabin@noao.edu
Received 1995 March 24; accepted 1995 September 28

ABSTRACT

We describe long-slit spectroscopy of the solar 4.7 μm carbon monoxide (CO) $\Delta v = 1$ bands at the Main spectrograph of the NSO McMath-Pierce telescope. We utilized stigmatic imaging of the temperature- and velocity-sensitive CO absorptions to map quiet regions near disk center and at the extreme limb. At Sun center the dominant long-lived spatial structures are small-scale hot spots associated with fragments of the supergranulation network seen in cotemporal Ca II filtergrams. Oscillatory thermal and velocity fluctuations of the global *p*-mode interference pattern are a pervasive feature of the maps, but the rms amplitudes ($\approx$70 K and $\approx$240 m s^{-1}) are perturbations on a relatively unstructured outer photosphere. We occasionally see small-scale transient cooling episodes—longer lived than the *p*-mode wavepackets—that might be overshooting granules or rising magnetic flux ropes. The events are too rare, however, to influence the global properties of the CO fundamental bands.

Seeing-selected frames of the off-limb CO emissions show a typical extension of 0".6 for the strongest lines, with little variation along the limb. The off-limb extensions indicate the presence of cool gas up to 350 km *above* the "$T_{\rm min}$" of popular reference models of the solar chromosphere.

We carried out two-dimensional model atmosphere simulations to study the effects of thermal inhomogeneities on the disk-center, extreme-limb, and off-limb behavior of the CO lines. The models are spherically symmetric, static, and in LTE. Our data favor a scenario in which the bulk of the low chromosphere—below the base of the magnetic "canopy"—is in reality a "COmosphere" dominated by gas colder than the minimum temperature in conventional models.

The moderate-scale ($\approx 5''$), mild thermal perturbations of the *p*-mode pattern have little influence on the CO $\Delta v = 1$ spectra. Small-scale ($\approx 1''$) hot regions embedded in a cool average atmosphere are strongly "shadowed" at the extreme limb. The shadowing is of little consequence, however, because the atmosphere already is dominated by the cool component. The opposite scenario—small-scale cold regions in a warm average atmosphere—can produce effective shadowing at the limb for granule-size ($\approx 1''$–$2''$) dark points only if the covering fraction is relatively large ($f \gtrsim 0.2$). That scenario is ruled out: it predicts high-contrast dark spots at disk center, contrary to our observations. We also argue against the possibility of shadowing by even smaller, subresolution ($\approx$0".3) cold spots with $f \gtrsim 0.1$.

We show that multistep reactions, rather than direct radiative associations, dominate the gas-phase chemistry of CO molecules under conditions typical of the outer photosphere. The CO formation and radiative cooling timescales are fast enough that low-temperature plasma conditions can be restored following disruption by a localized heating event such as a Ca II K$_{2V}$ "flash." In cool giant stars, the chemical formation timescales are much longer than in dwarfs like the Sun. Nevertheless, the density dependence is such that the molecular cooling proceeds proportionately more rapidly than the gas dynamics, ensuring an even more important role for autocatalyzed "thermal bifurcation."

Subject headings: Sun: abundances — Sun: activity — Sun: atmosphere — Sun: infrared —
Sun: oscillations

1. INTRODUCTION

The strong $\Delta v = 1$ (fundamental) vibration-rotation bands of carbon monoxide are denizens of the thermal infrared (near 2000–2200 cm^{-1}: 5.0–4.6 μm). The study of these bands in the solar spectrum has been provocative and controversial. Noyes & Hall (1972a, b, hereafter NH) reported curious "cool cores" ($T \approx 3700$ K) of strong CO lines near the quiet limb. Such temperatures are remarkable because they rival the *minimum* values in modern models of cold *sunspots* (Maltby et al. 1986, hereafter MACKKL). NH also noted a dramatic signature of the 5 minute oscillations in CO time series at Sun center.

At the time, a controversy raged concerning whether the solar minimum temperature was as hot as the 4400–4500 K indicated by the Ca II and Mg II wings (e.g., Ayres & Linsky 1976) or the somewhat cooler 4200 K suggested by far-ultraviolet and submillimeter continua (Vernazza, Avrett, & Loeser 1973). During the $T_{\rm min}$ debate, the anomaly of the earlier CO observations was overlooked. NH themselves attributed the dark cores of the strong $\Delta v = 1$ lines to the narrow, cool subduction lanes of the photospheric granula-

---

[1] Visiting Astronomer, National Solar Observatory, National Optical Astronomy Observatories, which are operated for the National Science Foundation by the Association of Universities for Research in Astronomy, Inc.

tion. The perversely cold CO thus was regarded as a minor oddity of the photosphere: of questionable relevance to the global atmosphere and certainly not germane to the overlying chromosphere.

In the late 1970s, a large Fourier transform spectrometer (FTS) was commissioned at Kitt Peak (Brault 1979). The $T_{\rm min}$ debate had rekindled interest in alternative spectral thermometers for the outer photosphere. Ayres & Testerman (1981, hereafter AT) finally reexamined the anomalous extreme-limb behavior of CO, confident that the new high-precision instrument would bring the $\Delta v = 1$ bands into line with other $T_{\rm min}$ proxies. Instead, AT not only confirmed the NH result but also showed that the riddle of the cold CO could be solved most naturally by *eliminating* the chromospheric temperature rise itself.

Ayres (1981) offered an explanation for the proposed radical surgery on the chromosphere. In the absence of significant mechanical heating, the outer atmosphere relaxes to a low-temperature state ($T < 3000$ K) close to radiative equilibrium (RE): mild photoabsorption heating in the H^- continuum is balanced by strong surface cooling in the CO $\Delta v = 1$ bands themselves. Wherever the local mechanical heating tops a critical level, however, the gas warms, and the CO molecules begin to dissociate. The loss of cooling power leads to additional warming and further dissociation. The ensuing "heating catastrophe" halts only at relatively high temperatures ($T \gtrsim 6000$ K), where cooling agents like Ca^+ and Mg^+ come into play.

Thus, the outer atmosphere of the Sun is "thermally bifurcated." It can exist in two distinct states—one cold, the other hot—depending on the amount of mechanical energy deposited locally. The mechanism is effective only at high altitudes. Once the CO $\Delta v = 1$ bands become optically thick, their near-LTE formation (Ayres & Wiedemann 1989, hereafter AW, and references therein) strongly suppresses the radiative cooling.

The CO-inspired revisionists thus relegated the classical hot chromosphere to small-scale overheated structures, bathed in a pervasive cool atmosphere close to RE. Although Mauas, Avrett, & Loeser (1990) challenged the simple analytical basis of the mechanism, the essential aspects of the CO-regulated thermal bifurcation have been validated in the static NLTE-blanketed RE solar simulations of Anderson (1989) and the model chromospheres with prescribed heating laws of Anderson & Athay (1989). Namely, very cool temperatures ($T < 3000$ K) are possible at high altitudes; the CO-cooled zone can survive low-level mechanical heating, but it disappears abruptly once the heating passes a critical level (e.g., Anderson & Athay 1989, Fig. 1). Furthermore, two-dimensional radiation/hydrodynamic simulations of convection demonstrated that the CO $\Delta v = 1$ bands can maintain a cold, horizontally uniform layer above the classical $T_{\rm min}$ in the face of the fluctuating granular radiation field and overshooting (Steffen & Muchmore 1988).

At the same time, the thermal bifurcation mechanism was recognized as one facet of the more general phenomenon of autocatalytic "molecular cooling catastrophes" (e.g., Stencel 1987). These operate in a diversity of cosmic environments: for example, promoting the fragmentation and collapse of molecular clouds (Glassgold & Langer 1976) and forging silicate grains in the bloated outer envelopes of red giants (Muchmore, Nuth, & Stencel 1987). Cuntz & Muchmore (1994) recently have published a detailed discussion of CO-driven radiative/thermal instabilities and additional examples of applications.

Further studies of thermal bifurcation on the Sun were hindered, however, by limitations of the McMath FTS, particularly the difficulty of achieving high temporal and spatial resolution (although the former deficiency was overcome to some extent in the CO oscillation work of Ayres & Brault 1990, hereafter AB). The central question of the thermal bifurcation work—Is the high-altitude gas truly pervasive?—could not be answered directly.

In 1992, the National Solar Observatory upgraded the 13.8 m vertical ("Main") spectrograph of the McMath-Pierce telescope, installing a large IR grating (salvaged, appropriately, from the mothballed instrument that NH employed for their pioneering CO studies). During tests on the refurbished spectrograph, W. Livingston of the NSO staff discovered the remarkable off-limb emissions of the CO lines. The pivotal observation showed directly that cool gas exists well above the altitude where conventional models place the chromospheric temperature inversion (Solanki, Livingston, & Ayres 1994, hereafter SLA). Still, the new work could not answer the key question concerning the surface coverage of the cool "COmosphere" (a term coined by G. Wiedemann). Given the long tangential sight line through the low chromosphere, even a small filling of cold gas could become optically thick in a strong CO line, yielding the off-limb emission signature.

Subsequently, a 256 × 256 Amber Engineering InSb camera and an image-stepping system (adapted from the NSO Near Infrared Magnetograph [NIM]: Rabin 1994) became available for use with the upgraded Main spectrograph. In 1993 October, Uitenbroek, Noyes, & Rabin (1994, hereafter UNR) utilized the hybrid instrument for long-slit imaging spectroscopy of the CO fundamental bands. Focusing mainly on the *p*-mode oscillations, UNR concluded that the evident patchwork quilt of spatial variations in the CO brightness is associated mostly with the oscillation interference pattern, particularly at high altitudes (i.e., as mapped in strong CO lines). That association strengthens the proposal in NH that the origin of the CO "cool cores" is largely dynamical, although Uitenbroek & Noyes (1994) make a connection with overshooting granules rather than the downwelling intergranular lanes suggested by NH. UNR found evidence that the dominance of the 5 minute *p*-mode period in Doppler shift gives way to a 3 minute period in line center intensity.[2] They also successfully imaged the off-limb extensions of the CO emissions in frames obtained during relatively good seeing, confirming the earlier descriptions by SLA.

Here, we report results from the second NIM/CO run. It occurred about 6 months after the first and incorporated several instrumental improvements. Appealing to two-dimensional atmospheric simulations and high-temperature gas-phase chemistry, we augment the work of UNR and advance in some respects an alternative interpretive viewpoint.

2. OBSERVATIONS

Our observing program took place during the week of 1994 March 21–25, although useful data were obtained only

---

[2] The effect noted in Fig. 2 of UNR is similar to that shown in Fig. 2*d* of AB; the higher frequency power is slightly more emphasized in the former, probably owing to the better spatial resolution of the NIM compared with the earlier FTS work.

1996ApJ...460.1042A

on March 22–24. The prevailing weather was intermittent cirrus and gusty winds. The seeing in the visible generally was poor, partly due to wind shake. Post facto evaluations of IR limb sharpness revealed typical conditions of 3″–4″, occasionally improving to 2″, or better, for brief intervals. The diffraction limit of the 1.5 m McMath-Pierce telescope is 0″.8 at 4.7 μm.

The NIM instrument configuration was similar to that described by UNR. We used a narrower entrance slit, 210 μm, corresponding to a projected width of 0″.5 on the Sun. The theoretical resolving power of the diffraction grating in second order is 1.1×10^5. UNR reported $\omega/\Delta\omega \approx 9 \times 10^4$ for their spectra (where $\Delta\omega$ is the FWHM of a Gaussian representation of the instrumental profile). However, our spectra show a much lower resolving power, perhaps only 4×10^4 (see below). In contrast, the FTS scans analyzed by AT and AB always exceeded 1.2×10^5, so that instrumental broadening was negligible for even the narrowest $\Delta v = 1$ lines.

Anamorphic transfer optics were used to match better the camera format to the telescope scale, yielding a field of ≈100″ with 0″.4 pixels (compared with 50″ and 0″.2 pixels during the 1993 October run). Unfortunately, one of the cylindrical lenses (since replaced) had optical aberrations that contributed to the lower spectral resolution and internal defects that caused localized fringing in the frames (which were a nuisance to flat field: see below). A 2.5 cm^{-1} interval of the spectrum was imaged on the detector, with 0.0092 cm^{-1} (1.3 km s^{-1}) pixels. A 50 cm^{-1} FWHM cold filter isolated the second order of the IR grating and suppressed thermal background.

A second improvement was a CCD system to take filtergrams in either Ca II K or Hα over a 2′.5 field surrounding the slit position. The cospatial CaK images allowed us to identify regions of persistent chromospheric brightness: supergranulation network or plages in the vicinity of spot groups. The Hα images were useful to distinguish quiet areas at the limb and active structures in the lower corona.

We operated the IR camera with an integration time of either 0.27 s or 0.14 s. The overhead of writing the frames to disk stretched the cadence to 3 s per exposure. We conducted two general types of experiments. The first involved progressively stepping the solar image across the slit to build up a large *spatial scan*, covering up to 2′ in 0″.5 strips. The second strategy was to step the image over a smaller field of view (typically 10″) but to repeat the sequence up to 100 times to build up a *movie*. The boustrophedonic (forward/backward) spatial scans yielded independent series of odd- and even-indexed images with a temporal spacing twice that for a single swath. With a width of 20 steps (10″), the effective repetition rate was one swath per 2 minutes. The cadence is too slow to document the fine details of the *p*-modes (as UNR did with long time series at a fixed slit position), but it does catch essentially the opposite phases of an oscillation between consecutive swaths. Further, the strip movies provide a two-dimensional view of the wave-packets (and other disturbances) unlike the one-dimensional picture afforded by a fixed slit. The trade-off reflects our main interest in the spatial structure of the solar surface that exists apart from the 5 minute standing waves.

We monitored the detector background by means of "hot dark" frames taken with the entrance slit shuttered. We also recorded pseudo–flat fields to correct the frames for pixel-to-pixel sensitivity variations and other instrumental artifacts (such as the fringing in the cylindrical lens described previously). We did not have a continuum lamp to illuminate the spectrograph slit uniformly at the same *f*-ratio as the solar image. We therefore used the Sun itself as the flat-field source. We accomplished this in two ways.

First, we obtained series of 10 frames during which a central portion of the solar disk was steered randomly across the slit to smear out discrete surface features. We then averaged the 10 independent exposures, imposing a "2 σ clip" through the stack to suppress anomalous points. Dividing the resulting "spatial flat" into a data frame successfully removes the pixel-to-pixel fixed pattern, but the "ratiogram" must be processed further to recover the desired spectral information.

A second flat-fielding technique was to widen the entrance slit until spectral lines were blurred beyond recognition. The larger area of the solar disk accepted into the spectrograph guaranteed a broad spatial average. Again, 10 frames were recorded and averaged. Dividing the resulting "slot flat" into a data frame removes the detector fixed pattern, restoring the innate stigmatic spectrum. However, the angular width of the slot was substantially larger than for the narrow observing slit, so secondary effects such as fringing and vignetting were not reproduced exactly. Thus, some artifacts survived the flat-fielding. We chose whichever pseudo-flat technique was most effective for each type of data, as described below.

Over the 3 useful days of the run, we accumulated thousands of IR frames, divided into dozens of observing experiments. We acquired large-field maps of quiet and active regions on the disk and long-duration movies over smaller strips. We recorded sequences at the solar limb using both radially oriented and inclined slits. The latter provide, as in UNR, better spatial sampling of the steep intensity roll-off at the edge of the disk, at the expense of reduced coverage inside the limb. Finally, we captured a rapidly developing surge at the east limb in the H I 7–5 (Pfβ) line at 2149 cm^{-1}. In the next section we consider only a severely pruned subsample of the best quality experiments.

3. DATA REDUCTION AND MEASUREMENT

The data sets we analyzed fall into two natural categories, for which we applied somewhat different reduction strategies.

3.1. *Disk Spectrograms*

First are the spatial scans and movies obtained on the solar disk, usually near heliocentric $\mu \equiv \cos\theta = 1$. Our objective was to measure the line shape parameters—velocity centroid, absorption depth, and Doppler width—along the slit for the important CO lines in the selected spectral region. We worked in two 2.5 cm^{-1} intervals, centered at 2143 cm^{-1} and 2149 cm^{-1}. The first contains a variety of weak and strong CO lines and is relatively free of telluric absorptions (e.g., NH, AB). The second holds fewer CO lines but includes Pfβ, a chromospheric signature that we hoped might help us spatially register CO maps against contemporaneous CaK or Hα frames. (In practice, however, the contrast of Pfβ on the disk proved too low to be of use.)

For the on-disk sequences, we corrected each data frame using a spatial flat, as described above. The resulting ratiogram contains spectral signatures related to the deviations of the local CO line shapes along the slit from the spatial/temporal average (cf. AT). The Amber camera is affected by flickering pixels that do not flat field well. We developed a mask for the most blatant of these and replaced the affected values in the ratiogram with a local median. We applied a minimal two-dimensional spatial filter (3 × 3 median followed by two passes of a 3 × 3 running mean) to the ratiogram to suppress any residual high-frequency artifacts. We verified—given the (low) 4×10^4 resolution of our spectra—that the filtering of the highly oversampled, low-contrast ratio map minimally affects the instrumental profile.

We then multiplied the cleaned ratiogram by a reference average spectrum to recover the intrinsic line shapes. One way to construct the average spectrum is directly from the spatial flat. For example, one could correct the spatial flat with the associated slot flat and then filter along the slit direction with a window large enough to clip residual artifacts, but small enough to preserve the mild spectral wiggles (due to optical aberrations) and a slight misalignment of the slit direction with respect to columns of the detector array. The reconstituted spectrum will suffer, however, from whatever telluric absorptions are impressed on the average spectrum: the advantage of their cancellation in the ratiogram is lost. Furthermore, any sensitivity variations across the detector that differ between the slot flat and the spatial flat (such as vignetting) will propagate into the recovered spectrum, again cancelling an important benefit of the ratiogram.

Therefore, we devised a second—somewhat adventurous—way to render the reference spectrum. First, we concocted a thermal model of the solar photosphere to match accurately the (highest resolution) FTS spectra in the 2143 cm^{-1} window, including the important isotopic transitions (cf. AW, Fig. 2). Next, we measured the centroids of five prominent CO lines in the spatial flat. The mean deviations along the slit provided a row-by-row zero-point offset of the wavenumber scale. Then we synthesized a theoretical two-dimensional spectrum from the model trace, degraded to the inferred 38,000 resolving power of the NIM and shifted by the appropriate zero point in each row. The resulting theoretical reference spectrum has no sensitivity variations along the slit and no telluric contaminations: the suppression of the two effects in the ratiogram carries over to the corrected frame. The procedure is equivalent to remapping the ratiogram into a form that can be measured using conventional absorption-line fitting techniques.

Figure 1 depicts a raw camera frame, the flat-fielded ratiogram, and the restored spectrogram via the indirect procedure. A trace from the central 16 rows is compared with the NSO FTS quiet Sun atlas (Livingston & Wallace 1991) and that of the Shuttle-borne ATMOS FTS (Farmer & Norton 1989). While the signal-to-noise ratio (S/N) in the processed NIM frame is high (several hundred), the spectral resolution clearly is significantly lower than either of the interferometers.

We measured the restored spectrograms by fitting Gaussian profiles to selected CO lines. We also assessed several continuum windows to derive reference continuum images and to check for drifts due to changing transparency or detector gain. Processing a frame yields a one-dimensional spatial distribution of CO line shape parameters (and continuum intensities). Sequences of one-dimensional fits can be concatenated into two-dimensional images of line depth, Doppler shift, and FWHM. The parameters derived from lines of similar strength can be averaged to enhance S/N.

Given, say, the residual depths of a CO line in a spatial map or movie, we calculated the deviation of each pixel value from the grand ensemble average. These deviations imply corresponding temperature fluctuations under the assumption of LTE formation (confirmed by AW to be an excellent approximation for the $\Delta v = 1$ bands). We caution

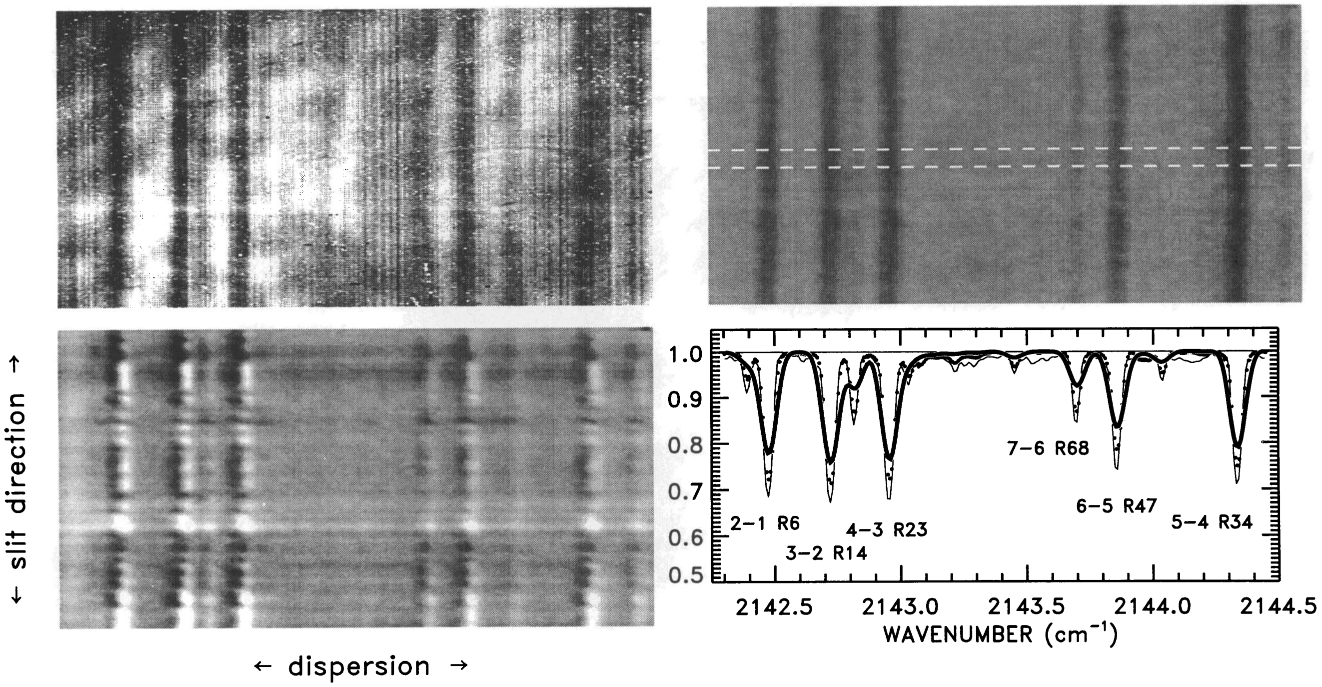

FIG. 1.—*Upper left:* 256 × 256 raw NIM spectrogram, compressed in slit direction; *lower left:* flat-fielded "ratiogram"; *upper right:* final spectrogram, cleaned and restored from the ratio; *lower right:* spectrum traced from central 16 rows (*thick curve:* $\omega/\Delta\omega \approx 3.8 \times 10^4$), compared to NSO FTS (*thin curve:* 2×10^5) and Shuttle-borne ATMOS FTS (*dots:* 9×10^4). Note that the telluric spectrum either has been compensated (NIM, NSO) or was absent in the original observation (ATMOS).

that the spatially averaged *absolute* temperatures derived from the CO lines here are several hundred degrees *hotter* than values from fully resolved FTS measurements (e.g., AT, AB). The discrepancy is due to the poorer spectral resolution of the NIM. Low resolution not only weakens the absorption lines but also can depress the apparent continuum level by promoting blending in crowded regions of the spectrum. Therefore, the NIM data are most useful for *differential* assessments of temperature.

Figure 2 depicts a thermal map of a 2′.0 × 1′.5 area near disk center recorded at 1910–1922 UT on 1994 March 24. The seeing was poor owing to gusty winds, but the sky was clear and the air mass was low (1.17). The CO map is an average of three strong lines from the 2143 cm^{-1} interval (2–1 R6, 3–2 R14, and 4–3 R23). The upper panel superposes three CaK maps obtained before and after the observation. The contours highlight bright features present in all of the CCD frames (over a time span of 20 minutes). The CO color table emphasizes surface features significantly brighter or darker than the average. Most of the CO map lies in the narrow temperature range ±200 K; only a small percentage is at the extremes. Many of the highlighted "hot" CO patches correspond to CaK-bright areas, apparently network fragments.

Figure 3 displays a movie sequence of a 10″ × 100″ strip, approximately centered in the area of the preceding spatial map, crossing the CaK bright points. Line-of-sight velocity is illustrated in addition to the temperature, averaged over the three strong CO lines as before. We provide the independent even (Fig. 3*a*) and odd (Fig. 3*b*) series; again the color tables emphasize the extremes. The velocity maps reveal the fluctuating 5″–10″ wavepackets of the 5 minute oscillation interference pattern. The temporal coherence is deemphasized here because the 2 minute repetition rate is slightly faster than the typical 2.5 minute half-period of the dominant *p*-modes. The relationship between the temperature and velocity maps is consistent with the conclusion that the disturbances are predominantly adiabatic (e.g., AB).

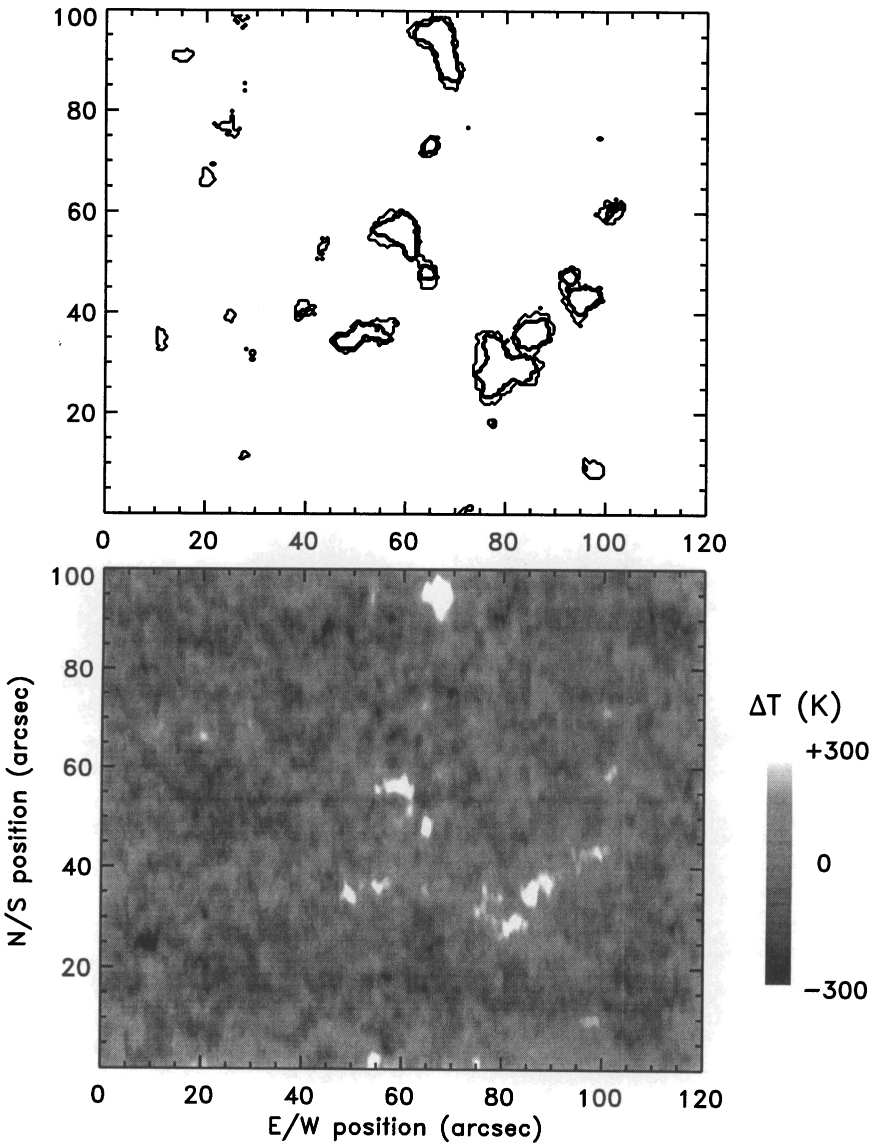

FIG. 2.—*Lower panel:* thermal map of a 2′.0 × 1′.5 area of quiet Sun near disk center, based on three strong CO absorptions from the 2143 cm^{-1} interval. The color table emphasizes features hotter or cooler than typical of the *p*-mode interference pattern. *Upper panel:* cotemporal CaK map from a superposition of three CCD images. Closed contours outline the bright areas—mostly network fragments—that persisted during the 20 minute duration of the CO spatial scan.

1996ApJ...460.1042A

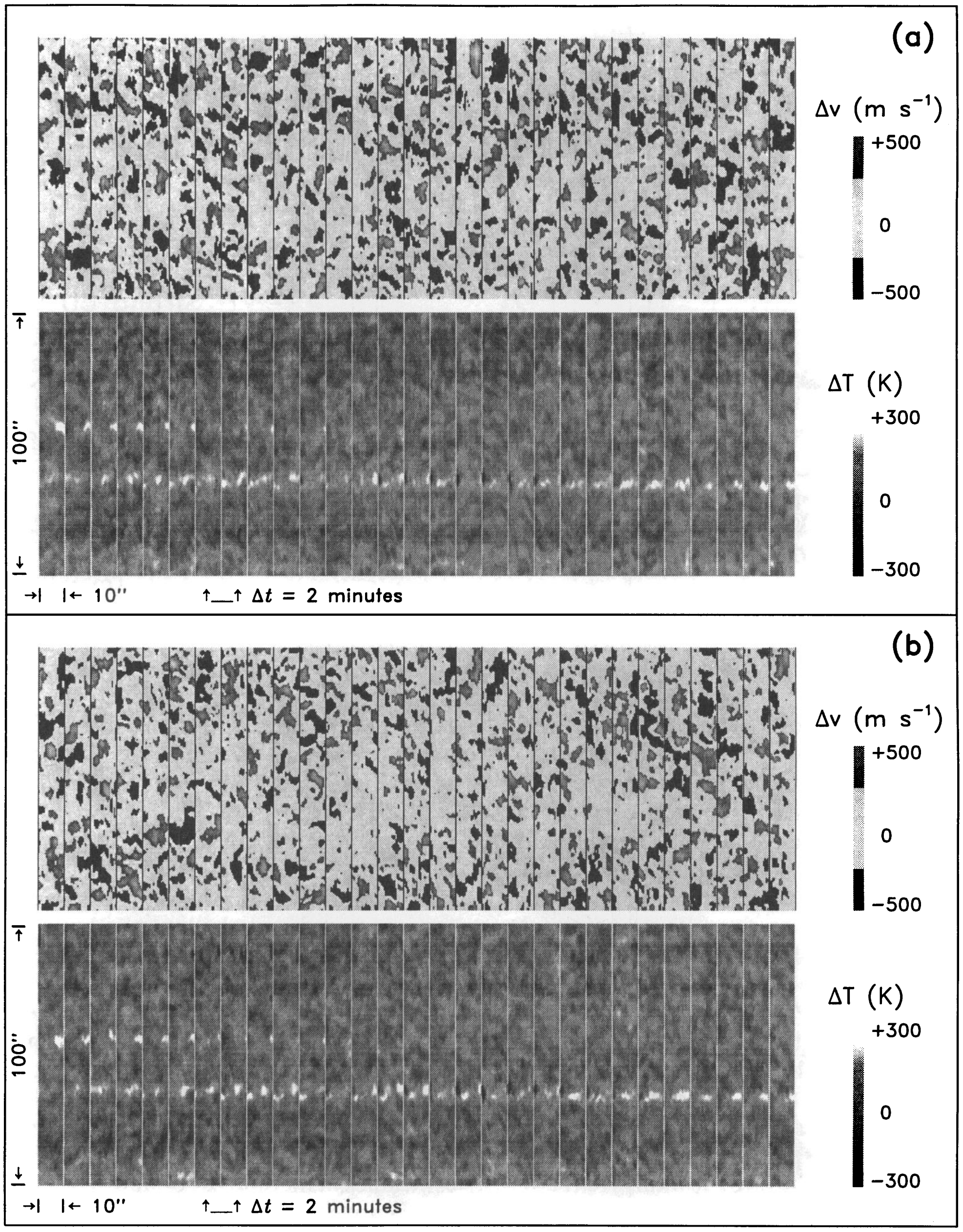

FIG. 3.—(*a*) Reverse (even-numbered) strips from a boustrophedonic movie sequence. *Upper panel:* Doppler velocities based on three strong CO lines. *Lower panel:* corresponding thermal fluctuations. The color tables emphasize the extremes. Each strip is 10″ × 100″, and the temporal spacing is about 2 minutes. (*b*) Same as (*a*) for the forward (odd-numbered) scans.

Persistent bright points associated with network fragments are apparent, as in Figure 2. Occasionally one also sees a small-scale dark point that survives for 6–10 minutes, far longer than the average *p*-mode quarter-cycle lifetime. These events are not accompanied by unusual vertical velocity signatures, although their size (≈few arcsec) is compatible with overshooting granules. They might be the "dark whiskers" seen in high-resolution studies of the Ca II wings by Beckers & Artzner (1974) or perhaps the tiny "invisible sunspots" noted by Zirin & Wang (1992). Title et al. (1995) recently described small-scale darkenings in very high spatial resolution filtergrams of the CH G-band near 430 nm. They attribute the events to rising—predominantly horizontal—magnetic flux ropes. In all cases, the cooling disturbances are rare.

Figure 4 illustrates temperature and velocity histograms based on the preceding movie for the average of the three strong lines and for (weak) 7–6 R68. The distribution functions are typical of those observed in several quiet regions. The rms widths ($\Delta T = 70$ K and $\Delta v = 240$ m s^{-1}) of the strong-line histograms are somewhat smaller than reported by UNR but are in agreement with the FTS results of AB (for their "SOL25" experiment: a 43 minute time sequence through a 5″ aperture). The lower spectral resolution of the NIM should suppress ΔT relative to the FTS by about 40% but should have a lesser influence on Δv. The contribution of the higher spatial resolution of the NIM is uncertain but probably minimal, given the relatively large coherence length of the *p*-mode wavepackets. Better spatial resolution might, however, at least partially balance the influence of the spectral degradation. Figure 4 also offers contour diagrams pitting ΔT against Δv. The relations are elliptically

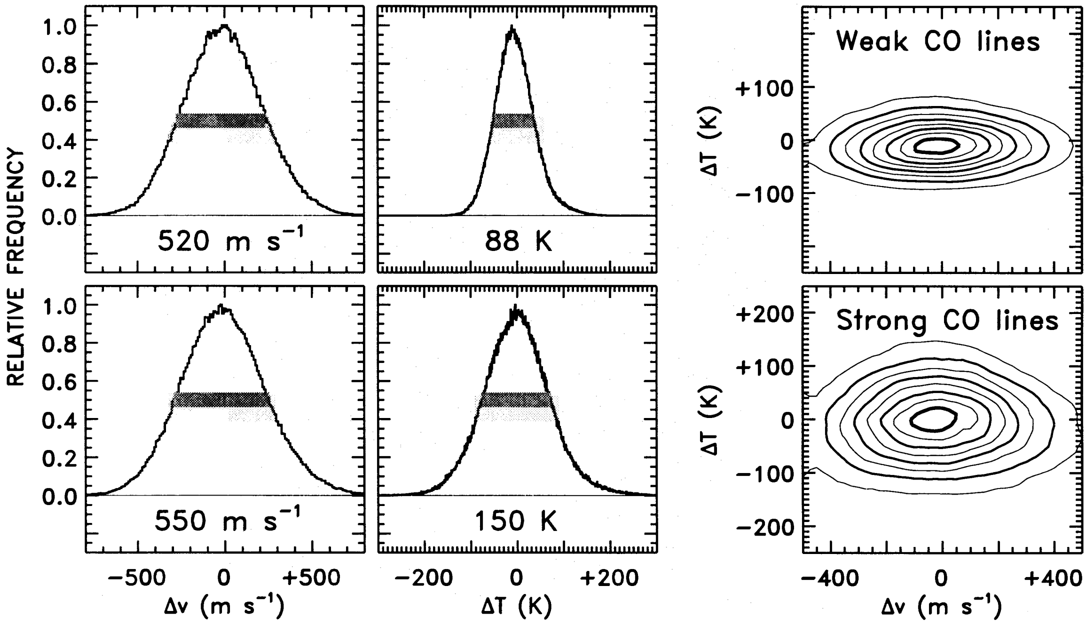

FIG. 4.—Histograms of temperature and velocity fluctuations based on the movie of Fig. 3 and joint ΔT vs. Δv contour diagrams. Shaded horizontal bars and numerical entries indicate FWHMs of the distributions. *Lower panels:* histograms for average of three strong CO lines. *Upper panels:* histograms for (weak) 7–6 R68.

symmetric, as expected for evanescent, near-adiabatic waves like the *p*-modes (for which temperature and velocity fluctuations are about a quarter-cycle out of phase: see, e.g., AB). There is no evidence for any systematic correlation between ΔT and Δv. We conclude that the thermal and dynamical perturbations of the outer photosphere are dominated by the *p*-mode pattern. The network bright points, and the small-scale cooling episodes of unknown origin, represent only minor populations.

3.2. *Limb Spectrograms*

The second general class of observing experiments involved the solar limb. Here, the ratio technique is less useful because the character of the spectrum changes rapidly along the slit. Indeed, our primary interest was the degree of extension—with respect to the continuum edge—of the CO lines in emission above the limb. We therefore corrected the limb frames with a suitably prepared slot flat, accepting the possibility of low-level residual artifacts.

We did not spatially filter the restored images, in order to maintain the highest possible spatial and spectral resolutions. The former criterion is obvious owing to the relatively small limb extensions of the CO lines: comparable to the diffraction limit, but easily measured as a differential effect. The second criterion is less obvious, but low resolving power not only weakens the absorption line in the disk spectrum but also depresses the central intensity of the off-limb emission feature. Both effects conspire to push the apparent half-power point *inward* toward the limb, trimming the off-limb extension. Even a small influence can be significant: a radial offset of only 0".1 corresponds to one scale height at the top of the photosphere.

A secondary objective was to construct spatial maps to assess the thermal "rugosity" at the limb. The near-limb spatial contrast is an important discriminant between two opposing scenarios (described in § 4) to explain the anomalous limb darkening of the strong CO lines.

We thus processed the corrected limb images using two general strategies: one geared toward an accurate determination of the limb extensions and the other toward reliable spatial mapping. We selected promising frames from the several thousand limb exposures by applying an edge sharpness test.

In practice, we measured the absolute gradient of the intensity profile at the limb. When the gradient trace is narrow and peaked, the limb is sharp; when the gradient trace is broad and shallow, the limb is diffuse. Sometimes the gradient profile is doubled, indicating an abrupt displacement during the exposure (due to image shake, for example). After examining a representative sample, we developed a sharpness metric based on the apparent width, peak height, and asymmetry of the gradient trace. We constructed histograms and time series of the metric for the limb sequences. The histograms enabled us to isolate the globally best values of the metric, a guide to the few, sharpest frames. The time series allowed us to identify strings of consecutive exposures for which the edge definition exceeded a critical limit. We then could assemble such sequences into minimally blurred strip images of the extreme limb. Figure 5 portrays the sharpness metric for a series of limb observations on 1994 March 23, showing how the IR seeing improved during the course of that morning.

3.2.1. *Limb Extensions*

Having culled out a dozen of the sharpest frames, we measured the apparent monochromatic extension of the limb for the 256 frequency bins (columns) of each spectrogram. The selected data sets were obtained with radially oriented slits as well as inclined slits. For both types, we established the intensity half-power point in a continuum window, traced the average spectrum at 3".5 ± 1".0 beyond it (i.e., well off the disk), and subtracted that level uniformly from the frame to compensate for stray light. Next we traced the average spectrum 7".5 ± 2".5 inside the limb ($\mu \approx 0.10$–0.15), dividing it into the stray-light corrected frame to normalize the intensities (and compensate for telluric absorptions). Then, using linear interpolation, we evaluated the displacement of the intensity trace at 60%, 40%,

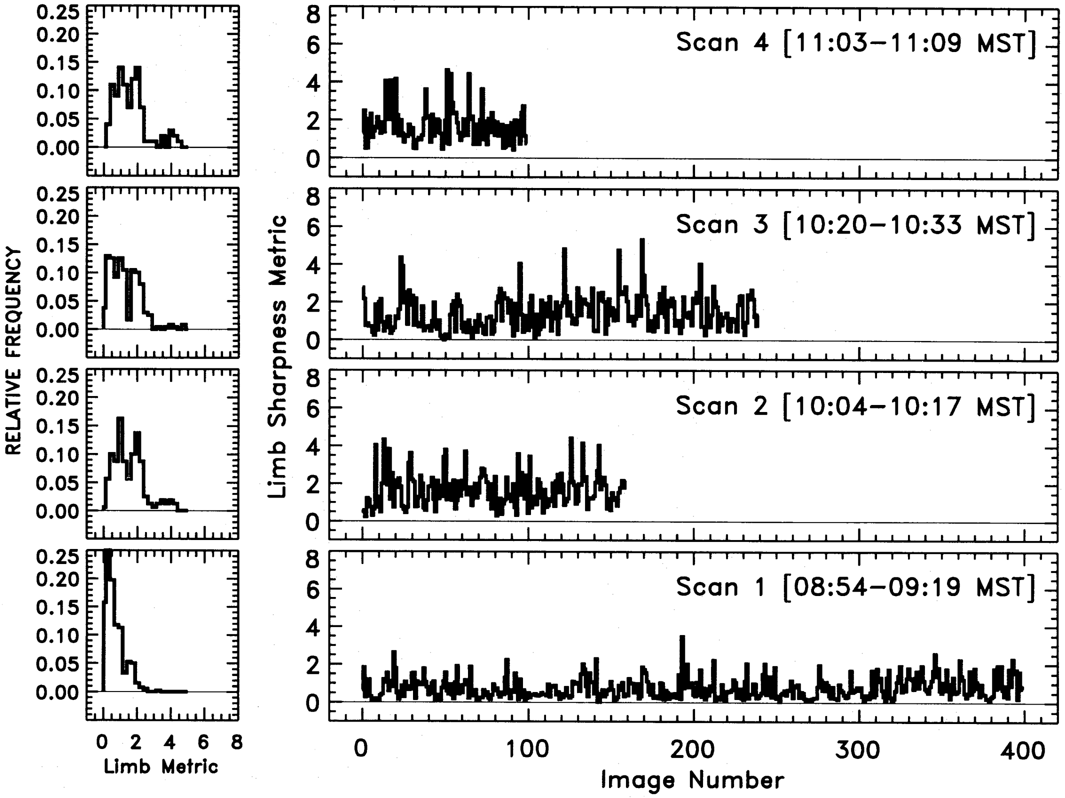

FIG. 5.—Histograms and time series of limb sharpness metric for four sequences taken during the morning of 1994 March 23. The apparent IR seeing was best close to local noon (scan 4), as reflected in higher values of the metric.

and 20% of the on-disk reference level in each column of the frame. Figure 6 provides particularly good examples. For the radially oriented slit (Fig. 6*a*), one can see the effect of the previously mentioned slight tilt (about 1 pixel in 256) of the spectrum. For the inclined slit (Figs. 6*b* and 6*c*), the tilt is less evident (owing to the effective radial minification of the pixels).

Figure 6 indicates that the extension of the strongest CO lines is 0''.6 and 0''.3 for the weaker lines. The H I Pfβ emission reaches a full 3'' beyond the continuum limb. The CO and H I extensions are independent of location, at least given our restriction to quiet areas and the few sharpest frames (out of several thousand) we analyzed in detail. Our conclusions are similar to those of Clark et al. (1995). They used the NIM during the 1994 May partial eclipse to record residual CO (and H I) emissions as the sharp lunar edge progressively covered the solar limb. Such an observation circumvents seeing (and the 0''.8 diffraction limit of the McMath-Pierce) but still can be affected by spectral resolution and scattered light. We discuss the implications of the CO off-limb extensions later.

3.2.2. *Extreme-Limb Spatial Structure*

In the second type of limb analysis, we selected strings of consecutive frames for which the seeing was uniformly better than a prechosen limit. We confined our attention to observations made with a radially oriented slit. Here, we measured the Gaussian parameters for selected CO lines, concatenated them into maps as described previously, and scaled the fluctuations in the parameters relative to their average values 20'' ± 2''.5 inside the continuum limb (corresponding to $\mu \approx 0.2$).

Our objective was to search for thermal fluctuations at the extreme limb, and the accompanying spatial scales, for comparisons with two-dimensional model simulations. We were fortunate in a few instances to have two or more good strip images at the same limb position, separated in time by several minutes or more. Such repetitions can indicate crudely whether specific limb structure is persistent or transient, again an important issue in confronting model simulations with reality.

Examples are illustrated in Figure 7. The extreme limb exhibits a spatial morphology superficially similar to that of disk center. The temperature excursions from the mean are relatively small, the fluctuations have a size typically several arcsec perpendicular to the slit, and most of the structure appears to change with time.

4. NUMERICAL MODELING

We conducted a series of numerical experiments in the spirit of the two-dimensional simulations exploited by AT to interpret the early FTS spectra. The CO problem is particularly advantageous because the $\Delta v = 1$ bands form essentially in LTE (AW), as do the dominant continuous opacities: free-free transitions of H^- and H (Vernazza, Avrett, & Loeser 1981). That simplification allows one to undertake simulations with a significant amount of geometrical complexity that otherwise would be forbidding for NLTE scattering lines.

One effect that deserves special attention is the possibility that small-scale ultracold structures could skew the average temperatures of the CO cores near disk center and perhaps dominate the extreme-limb behavior through *shadowing.* The accurate treatment of near-limb shadowing requires the solution of a two-dimensional radiative transfer problem in a curved, highly structured, thermally inhomogeneous atmosphere. The near-limb shadowing problem is closely

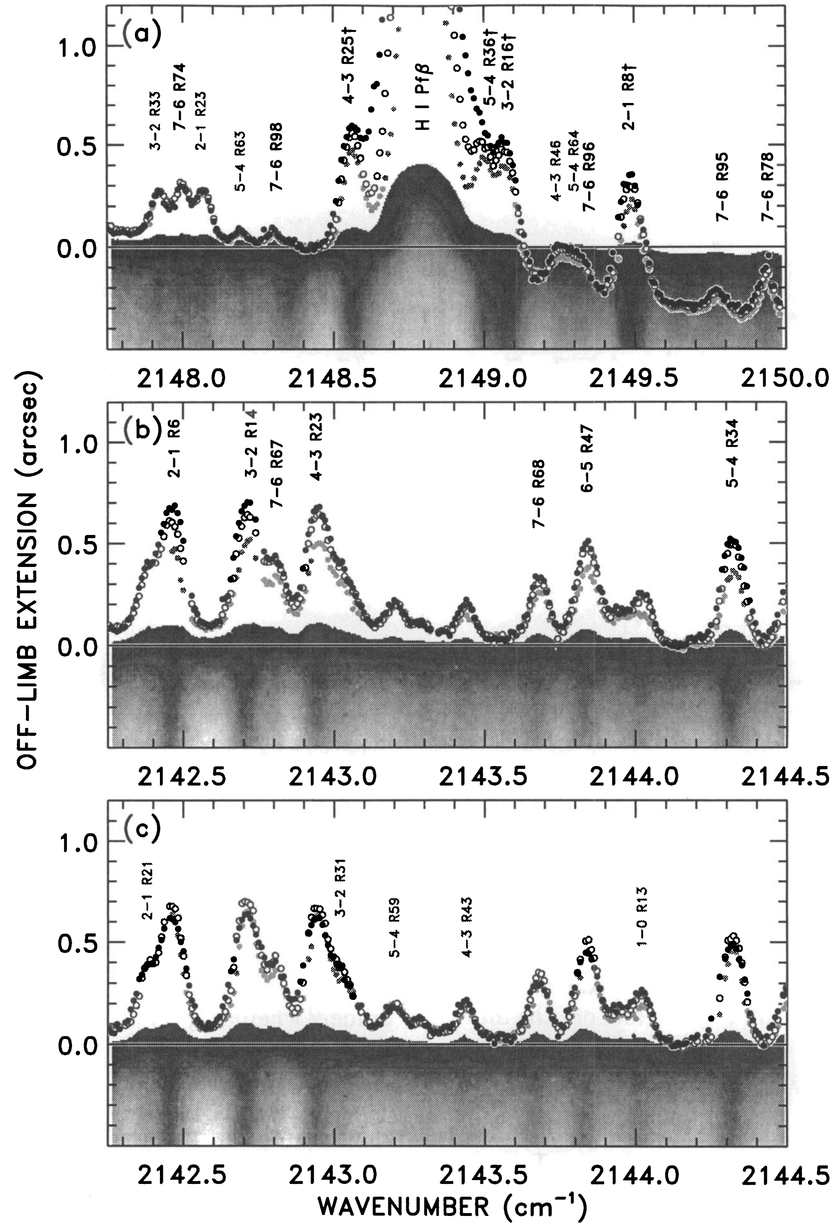

FIG. 6.—(*a*) Extensions of CO and Pfβ emissions above the limb in the 2149 cm^{-1} interval at 60% (*light dots*), 40% (*open circles*), and 20% (*dark dots*) of the on-disk intensity at that frequency (relative to the displacement of a continuum window at the corresponding intensity level). The dots are superimposed on a gray scale representation of the spectrogram (the latter is not to scale in slit direction). Prominent CO lines are indicated: ^{12}C ^{16}O (*dark annotations*); ^{13}C ^{16}O (*lighter annotations*); daggers mark blends. The frame was 126 in a sequence taken at the north limb with a radial slit on 1994 March 23. (*b*) CO emissions in the 2143 cm^{-1} interval; frame 46 in a sequence taken at the east limb with an inclined slit on 1994 March 24. (*c*) Frame 48 in the same sequence as (*b*).

related to that of the off-limb extensions of the CO lines. It seemed natural to treat them together in a unified simulation.

4.1. *Spatially Averaged Properties*

Before we describe the details of the modeling procedure, we recall from the FTS work the spatially averaged properties of the CO bands that a viable model, homogeneous or not, must replicate. The accessible vibration-rotation transitions span a wide range of excitation energies and oscillator strengths and, thus, a wide range of formation heights, a property shared with the extensive damping wings of the Ca II H and K lines (e.g., Ayres 1975). On the one hand, the weaker, deeper lying CO $\Delta v = 1$ features have disk-center core brightness temperatures consistent with models developed to match the photospheric damping wings of atomic and ionic transitions (Holweger & Müller 1974 ; Ayres & Linsky 1976; MACKKL). On the other hand, the stronger CO lines exhibit disk-center core temperatures several hundred degrees *cooler* than indicated by the—again, spatially averaged—Ca II wings (see, e.g., AT, AB). At the extreme limb ($\mu \lesssim 0.2$), the weaker CO lines show spatially average temperatures comparable to the stronger CO lines *at disk center*, while the strong CO lines reveal the anomalous dark cores (as low as 3700 K) noted by NH. At disk center, the strong $\Delta v = 1$ lines have Doppler FWHMs of about 6 km s^{-1}, while the weaker lines are somewhat narrower (FWHM $\approx$ 5 km s^{-1}). At the limb, the FWHMs are about 7.5 km s^{-1} and 6 km s^{-1}, respectively. The widening of the lines toward the limb could be due to opacity

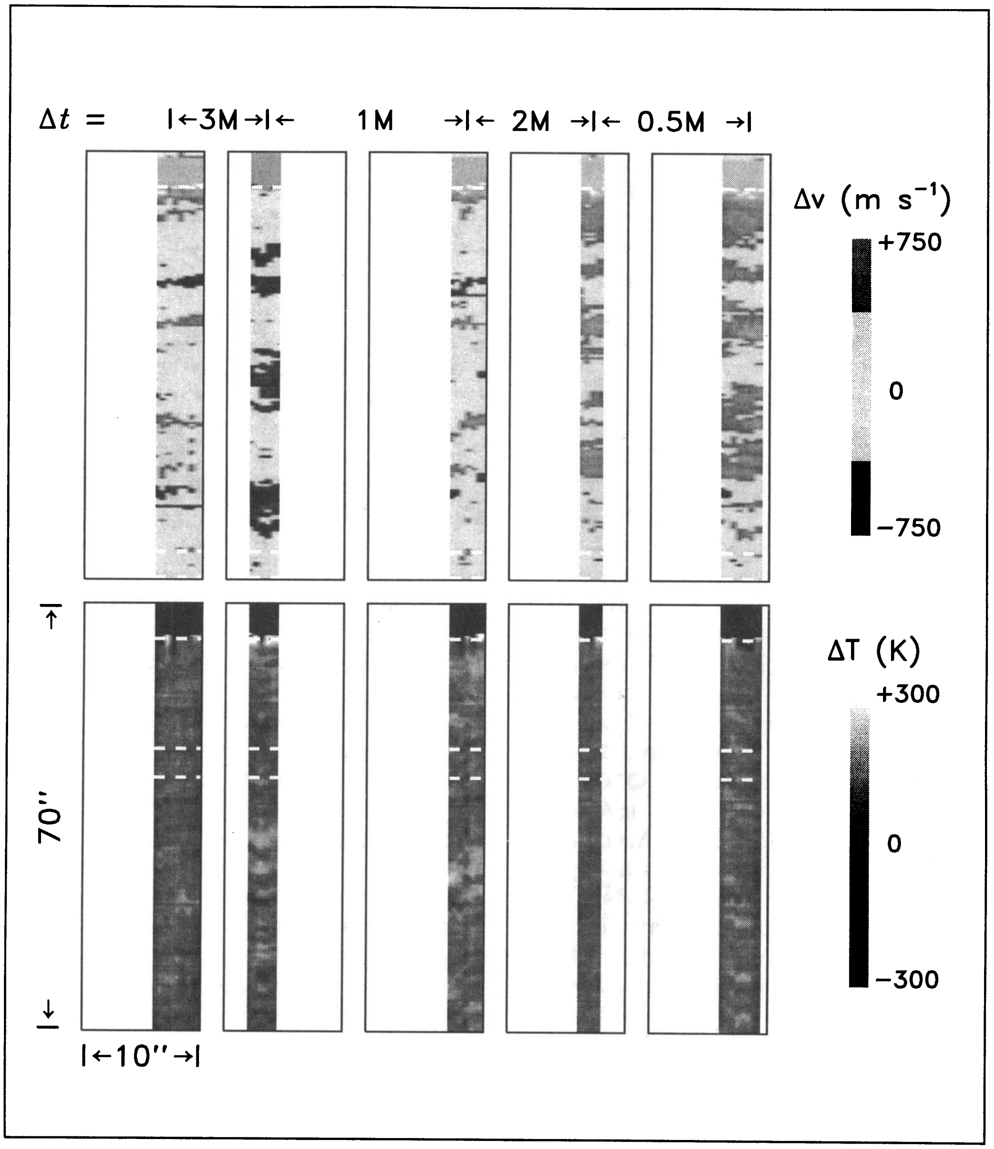

FIG. 7.—Excerpts from a movie taken at the north limb with a radial slit on 1994 March 23. Dark rectangles outline full 10" × 70" of each strip, within which are illustrated only the consecutive frames that exceeded a minimum limb sharpness criterion. The thermal maps were normalized to the average temperature in the narrow zone outlined by white dashes ($\mu \approx 0.2$), while the velocity maps were normalized to the average at the bottom of each frame. Time intervals separating the different strips are given at top.

broadening, a rise in the nonthermal Doppler velocities with altitude, an increase of ξ_t with viewing angle, or a combination of effects.

The weaker fundamental lines form in the same deep layers as the $\Delta v = 2$ first-overtone bands (near 2.3 μm). The latter can be used to set the carbon and oxygen abundances, and the microturbulent broadening, for any adopted photospheric model (e.g., AT, AB).

4.2. *A Reference Model*

We adopt a reference $T(h)$ stratification that has been adjusted to duplicate visible and near-IR absolute disk center irradiances and limb darkening curves. It provides (via the CO $\Delta v = 2$ analysis) carbon and oxygen abundances of 4×10^{-4} and 8×10^{-4}, respectively (on the scale where $A_{\rm H} \equiv 1$). A similar carbon abundance is indicated by studies of IR vibration-rotation spectra of the CH molecule recorded by the ATMOS instrument (Grevesse et al. 1991). The reference model also predicts the 2150 cm^{-1} continuum intensity that scales the residual intensities of the CO $\Delta v = 1$ absorptions to absolute core temperatures (see AB). We thus calibrate several crucial aspects of the observations and ancillary atmospheric parameters (e.g., abundances and nonthermal broadening) with respect to the (hopefully) well-established properties of the deep photosphere. There, the thermal inhomogeneities arise largely from small-scale fast convective processes and are strongly mitigated in spectra of low spatial and temporal resolution. The layers of the middle and deep photosphere are well removed from the high-altitude zone where thermal bifurcation becomes possible.

We extend the reference model into the higher layers following an upper photosphere thermal profile in accord with the Ca II and Mg II damping wings. We complete the reference model by splicing in a provisional chromospheric temperature inversion like that of the VAL C′ of MACKKL. The final reference model is similar enough to VAL C′ that we designate it as such, even though the thermal structure might deviate slightly in its details. In the inhomogeneous simulations, we adopt our incarnation of the VAL C′ as the "hot" component and treat the "cold" component as a modification of it.

4.3. *Two-dimensional Spectral Simulations*

We carry out the two-dimensional spectral simulations as follows. We consider a radial slice of the solar atmosphere along an arc of a great circle that includes the limb. We specify the two thermal components—"hot" and "cold"—and array them in an alternating repetitive pattern. We treat the atmospheres as static, apart from an internal nonthermal (microturbulent) velocity, ξ_t, included as a dynamical pressure term ($\frac{1}{2}\rho\xi_t^2$: Vernazza et al. 1973) and in the Doppler broadening of the CO lines.

The static assumption is pragmatic, given the considerable numerical complexity introduced by a fully dynamic simulation (cf. Carlsson & Stein 1994, hereafter CS). Nevertheless, it is vindicated by the lack of obvious organized vertical flows in our CO maps. Further, the amplitudes of the oscillating temperature and velocity fields are small enough that they represent only minor perturbations of the hydrostatic equilibrium. Optical studies of correlations between absorption-line Doppler shifts and intensity fluctuations suggest that the convective velocity field dies out in the middle photosphere, only a few hundred kilometers above $\tau_{500\,\mathrm{nm}} = 1$ (e.g., Komm, Mattig, & Nesis 1990, and references therein). Two-dimensional gasdynamic simulations of convection including high-altitude CO cooling show that the granular fluctuations are minimal beyond an altitude of 350 km above $\tau_{500\,\mathrm{nm}} = 1$ (Steffen & Muchmore 1988). Furthermore, the piston-excitation numerical experiments of CS—calibrated against observed Doppler shifts of a midphotospheric absorption line—predict that the oscillatory velocity amplitude does not reach a significant fraction of the sound speed until at least 300–400 km *above* the conventional T_{min}. Perhaps not coincidentally, that is the level at which the CO off-limb emissions fade and the thermal structure probably returns to a "normal" chromospheric configuration. While hydrostatic equilibrium might be a poor assumption in the hot layers of the middle chromosphere, regulated by acoustic shocks (or other modes of excessive heating), it should be a much better assumption in the subcanopy zone, where the "cool clouds" of the COmosphere reside.

Given the temperature profiles of the hot and cold components, we derive the runs of densities with altitude by invoking hydrostatic equilibrium, LTE ionization equilibrium for the metals, and chemical equilibrium for the important diatomic molecules. We treat departures from LTE in hydrogen using a simple model of photoionizations in the Balmer continuum specified by a fixed rate (e.g., Linsky 1968). We then solve the LTE transfer problem along the line of sight, from a starting position on the projected disk approximately 20,000 km inside the limb ($\mu \approx 0.23$) and continuing in fixed steps (typically 100 km) to about 1500 km outside the limb. The ray solution begins at the intersection between the line of sight and the outermost radial point of the model. The latter is chosen in the high chromosphere—well above the thermally bifurcated zone—where the cold models have been forced to smoothly join VAL C′. The transfer proceeds inward in uniform steps (typically 20 km) until either the integration path becomes very opaque ($\tau \gtrsim 10$) or it reaches the midpoint of a translucent grazing ray. A semi-infinite boundary condition is applied in the former situation; the latter is treated in the finite-slab approximation. Opacities, emissivities, and Doppler profiles are determined at each step on the ray by interpolations from the component models, whichever is intersected at that point (according to the radial extension of the underlying pattern). CO line parameters—E_{VJ}, log *gf*, and partition functions $Q(T)$—are taken from the recent compilation by Goorvitch (1994).

We do not impose horizontal pressure equilibrium across the boundaries between the distinct thermal components. Initially we did so (see AB) by adjusting the microturbulence ξ_t in the cool component to compensate—via the dynamical pressure term—for the thermal overpressure of the hot component. However, the resulting synthetic CO line shapes were much broader than observed *above* the limb, so we set aside the assumption of dynamical pressure balance. We imagine, therefore, either that the cool zones are physically insulated from the hot gas—because, for example, the latter is magnetically confined in isolated chromospheric flux tubes—or that the cool zones exist in a state of dynamical disequilibrium that nevertheless evolves on relatively long timescales. We assumed a height-independent $\xi_t = 1.5$ km s^{-1} in the VAL C′ and in the upper photospheres of the cool-component models. We imposed $\xi_t = 2.5$ km s^{-1} in the COmospheric zones of the latter to help explain the additional CO line broadening apparent in the near-limb FTS scans.

Figure 8*a* illustrates the degenerate case of a single component, here the "hot" VAL C′ model. The simulated stigmatic spectrogram shows no spatial structure, as expected, except for slight off-limb extensions of the CO lines. The 2150 cm^{-1} continuum becomes tangentially optically thin at an equivalent radial height of $h \approx -350$ km; the CO populations in the T_{min} region of VAL C′ (up to $h \approx -550$ km) still are large enough to yield optically thick tangential rays out to ≈0″.3 beyond the continuum edge. The companion Figure 9*a* depicts the predicted behavior of the CO core intensities at disk center ($\mu = 1$) and the extreme limb ($\mu \lesssim 0.2$). While the synthesized center-to-limb behavior of the weak 7–6 R68 absorption is consistent with that observed, the predicted strong 2–1 R6 line is about 200 K too hot at disk center and about 1000 K too hot at the limb. The homogeneous VAL C′ model predicts a small amount of limb *brightening*, contrary to FTS observations. At the spectral resolution of our NIM frames and 1″ spatial resolution, the off-limb extensions of the weak and strong CO lines are only 0″.20 and 0″.35, respectively, significantly smaller than observed. The present simulations reiterate the inability of normal chromospheric models to duplicate the disk and off-limb signatures of strong $\Delta v = 1$ lines.

Figure 8*b* offers another realization of a thermally homogeneous atmosphere, one that *can* match the essential empirical properties of the CO bands. *COOLC* is identical to VAL C′ in the deep and middle photosphere but smoothly declines from the T_{min} of VAL C′ to a minimum of 3000 K at an altitude of $h = -850$ km. Between $h = -900$ km and -1000 km, the cool component has a steep temperature inversion of its own to rejoin VAL C′ in the chromospheric "canopy" (cf. SLA). In essence, COOLC represents a normal chromospheric temperature profile with the T_{min} elevated by 350 km (about five pressure scale heights) and chilled by 1500 K. It is something like a *cool cloud* on the underside of the hot chromospheric canopy of merged network magnetic fields (and/or dissipating acoustic shocks).

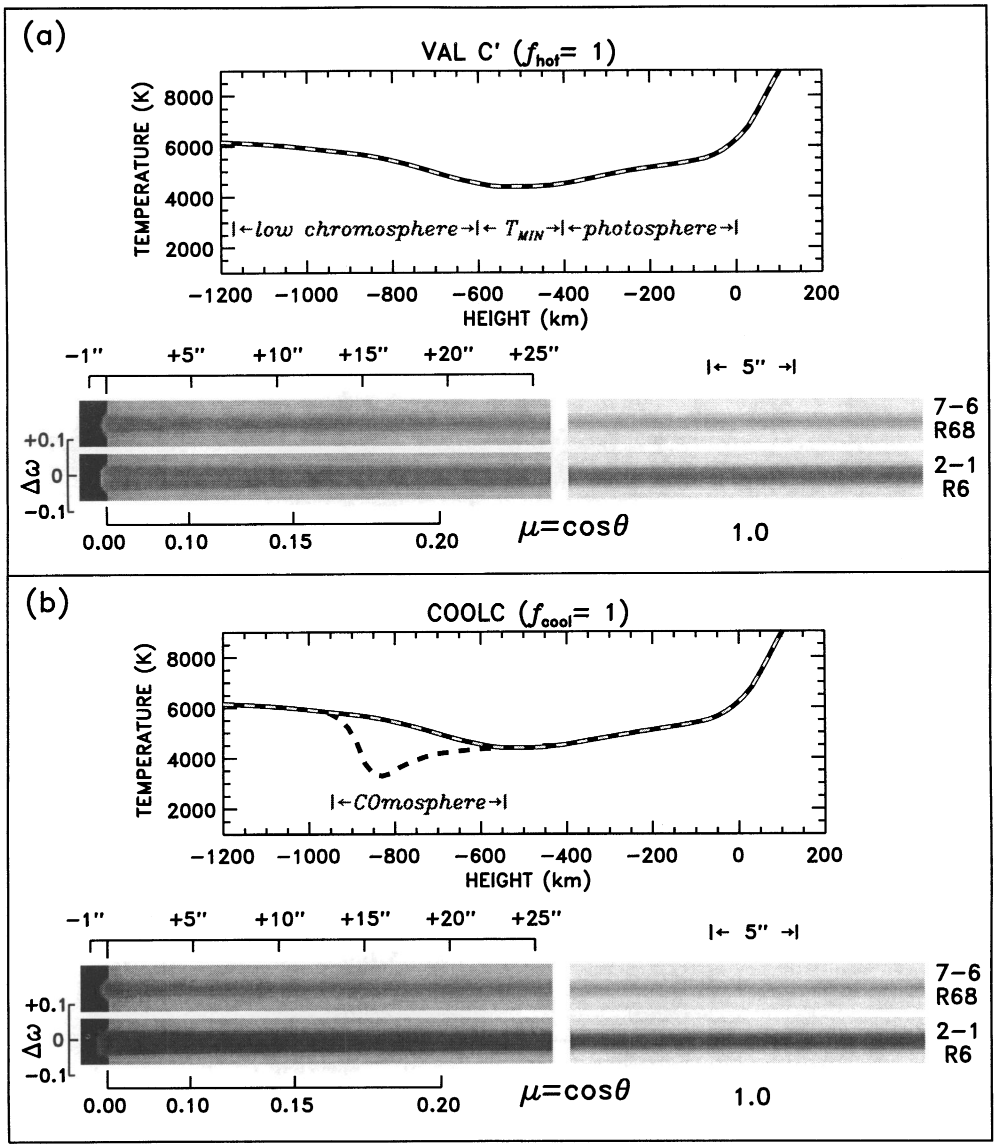

FIG. 8.—Thermal models and predicted CO spectrograms from two-dimensional numerical simulations. The lower half of each panel depicts a synthesized spectrogram in either weak 7–6 R68 (*upper frame*) or strong 2–1 R6 (*lower frame*): the limb is to the left; disk center is to the right. (*a*) Model and spectrogram for the VAL C′ reference atmosphere of MACKKL, distributed homogeneously across the surface. The $T_{\rm min}$ of 4400 K is located at an altitude of −500 km ($\tau_{500\ \rm nm} = 1$ defines the zero of the height scale). (*b*) Same as (*a*) for a single-component model ("COOLC"; *dashed line*) designed to match the CO $\Delta v = 1$ bands without regard to other (e.g., UV) signatures of the outer atmosphere. COOLC is identical to VAL C′ in the photosphere but departs significantly from the reference model above the $T_{\rm min}$ of the latter, falling almost 3000 K cooler at a height of −850 km. The COOLC thermal profile returns to the reference model at a "canopy" altitude of −900 km, however, in order to duplicate the observed truncation of the off-limb extensions of the strongest $\Delta v = 1$ lines.

The synthesized stigmatic spectra in Figure 8*b*, and the line-center traces in Figure 9*b*, show only very minor differences compared with VAL C′ in the weak 7–6 R68 absorption but obvious departures in the strong 2–1 R6 line. On the disk, 2–1 R6 is darker than in the VAL C′ simulation, and the darkening increases toward the limb, as observed. Above the limb, in Figure 9*b*, both the weak and strong $\Delta v = 1$ lines of COOLC show larger extensions (which have been brought into accord with the observed values—for NIM spectral resolution and 1″ spatial resolution—by adjusting the canopy altitude). While the homogeneous COOLC model is more successful in reproducing the spatially average CO properties than VAL C′, that success must be tempered by its inability to duplicate various UV diagnostics that clamor for a hot low chromosphere (e.g., Avrett 1995; but see also Lites 1994 for an alternative view).

Figure 10*a* illustrates a simple realization of a (mildly) inhomogeneous atmosphere designed to match the properties of the CO *oscillations* near disk center. Model OSC consists of two components, each a (slightly) perturbed version of VAL C′, with horizontal extents of 5 Mm (7″: 1 Mm ≡ 10^3 km = 1″.4) arrayed on 10 Mm centers, yielding a spatial filling of 50% for each component. The depth dependence of the thermal perturbation was adjusted to mimic the disk-center spatial rms brightness temperatures of 2–1 R6 and 7–6 R68, while the linear size of the components is that typical of the *p*-mode wavepackets in the CO thermal maps.

In Figure 10*a*, and its companion Figure 11*a*, the synthesized stigmatic spectra show the alternating brightness patterns at disk center, which persist even to the extreme limb. Nevertheless, the spatially average behavior of the CO

1996ApJ...460.1042A

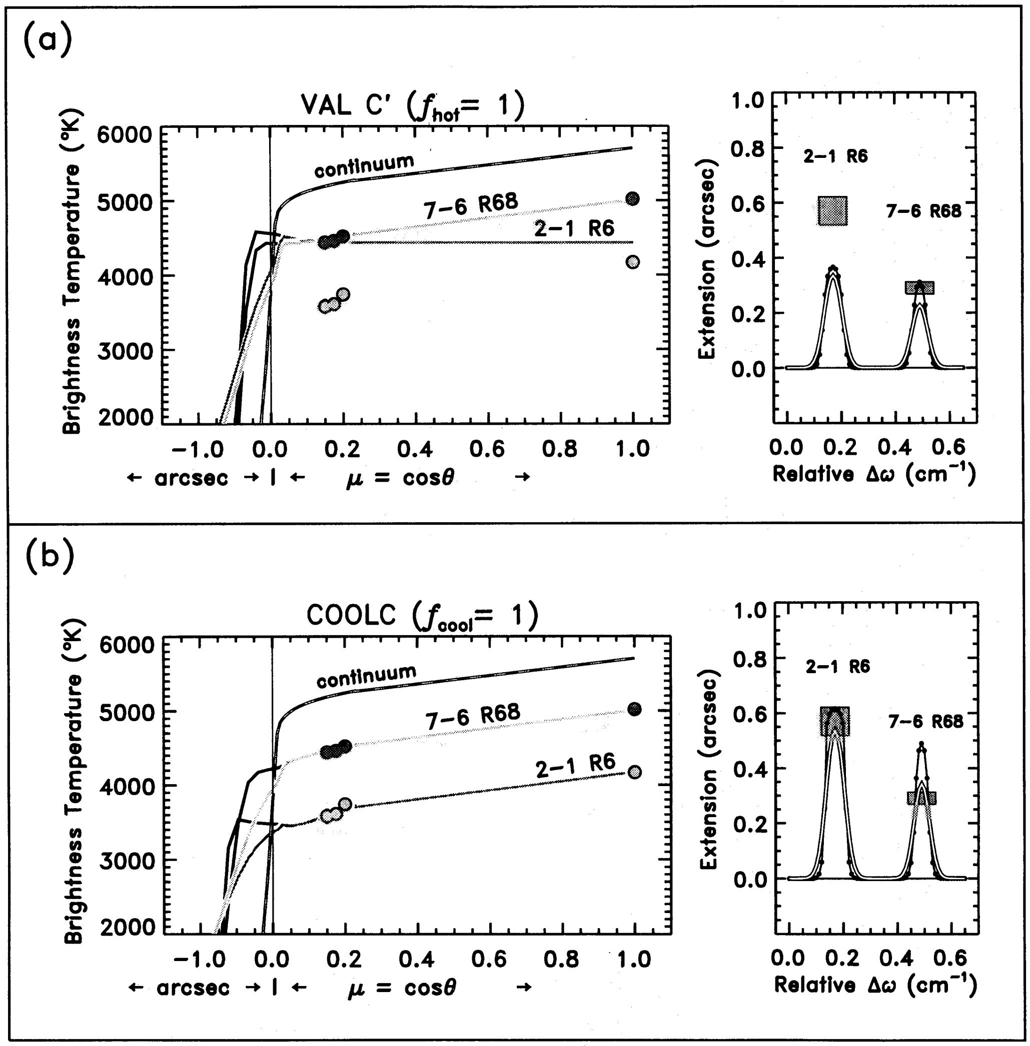

FIG. 9.—Predictions of the two-dimensional models—at disk center ($\mu = 1$) and at the extreme limb ($\mu \lesssim 0.2$)—compared with observations. *Left:* FTS measurements (*shaded dots*) of brightness temperature (spatially averaged but with high spectral resolution). Predicted spatial distributions of brightness temperature (for 2–1 R6 or 7–6 R68) are depicted by a dark curve (at "eclipse" resolution of 0″.2) and a lighter overlying curve for "best-NIM" resolution of 1″. *Right:* NIM-recorded off-limb extensions (*shaded boxes*, reflecting the range of values measured from seeing-selected frames). The model monochromatic extensions were calculated as in Fig. 6 (for the 40% intensity level), either at eclipse spatial resolution, with a resolving power of 7.5×10^4 and *no* scattered light (*connected dots*) or "best NIM" spatial resolution (1″), with a resolving power of 3.8×10^4 (*light curve*). (*a*) For the VAL C′ reference model. (*b*) For COOLC. In both cases, the spatial averaging affects only the off-limb extensions, since the intensity distributions from the homogeneous simulations are spatially smooth on the disk.

spectra is essentially identical to that predicted by the unmodified VAL C′, not a great surprise given the relatively mild thermal perturbations of the *p*-mode oscillations. Thus, thermal fluctuations of the (small) amplitudes and (large) spatial scales of the *p*-modes minimally influence the evaluation of a mean model from spatially average CO center-to-limb observations (which, in fact, point to a temperature profile like that of COOLC). An analogous conclusion was reached—albeit in the context of UV spatial intensity distributions, not necessarily related to *p*-mode excitations—by Vernazza et al. (1981). Namely, a mean thermal model can replicate the apparent mean spectrum of the spatial distributions of UV diagnostics observed at low resolution (≈5″). However, because the mean thermal profile (specifically in the low chromosphere) that successfully duplicates the CO $\Delta v = 1$ properties is so different from that which reproduces the mean UV behavior, it is clear that a viable "unified" model must incorporate extreme thermal profiles compared with the mild perturbations (≈ few hundred K) considered here for model OSC, or in the Vernazza, Avrett, & Loeser work.

Figure 10*b* illustrates one possible realization of an extremely inhomogeneous atmosphere that can match the CO properties and that has the possibility to mimic the behavior of high-excitation UV diagnostics as well. *Scenario Zero* consists of a hot component with a horizontal extent (Δx_{hot}) of 1 Mm arrayed on 5 Mm centers, yielding a filling fraction of 20% ($f_{hot} = 0.20$). The hot structures are embedded in a pervasive cool component ($f_{cool} = 0.80$) similar to COOLC (again, modified so that the composite model reproduces the spatially average CO properties). In the low chromosphere, at a height of −850 km, the two components of Scenario Zero differ by nearly 3000 K.

The synthesized stigmatic spectra in Figure 10*b* reveal only very minor differences compared with VAL C′ in the weak 7–6 R68 absorption but not so in the strong 2–1 R6 line. At disk center, the latter shows faint 1 Mm "bright points" corresponding to the hot component. The strong

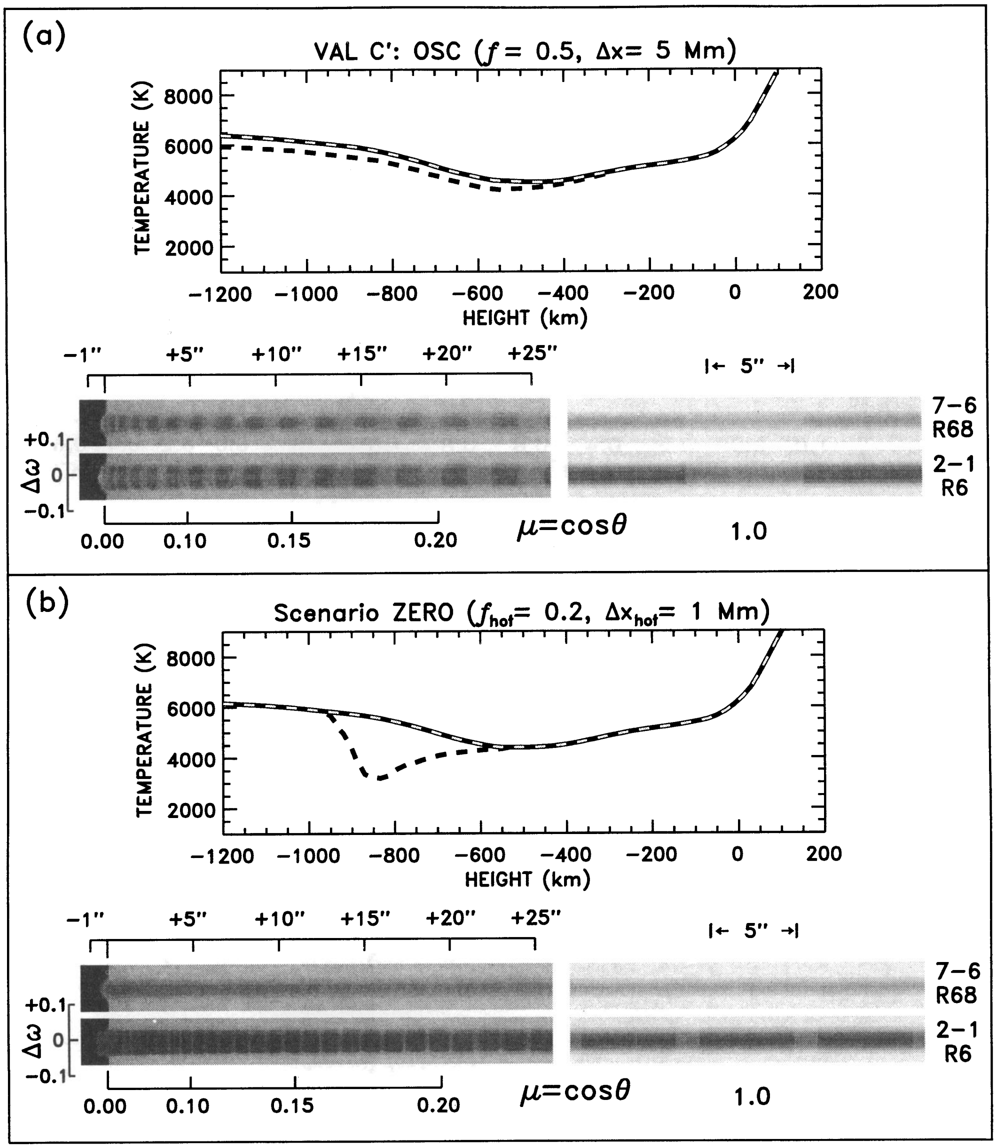

FIG. 10.—Same as Fig. 8, for explicitly two-component simulations. (*a*) Model "OSC": a pair of perturbed versions of the VAL C′ reference model, with a height-dependent ΔT designed to mimic the rms temperature fluctuations observed in the *p*-mode interference pattern (in weak and strong CO lines at $\mu = 1$). The components are arrayed in 5 Mm slabs on 10 Mm centers, comparable in size tc the typical *p*-mode wavepacket. The repetitive pattern is clearly visible at disk center and at the limb. (*b*) "Scenario Zero": a two-component model with 20% coverage of the VAL C′ (in 1 Mm wide slabs on 5 Mm centers) and 80% coverage by a "cool cloud" structure similar to the COOLC profile of Fig. 8*b*. Note the strong shadowing of the minority hot component in the synthesized limb stigmatic image of 2–1 R6.

CO lines reach radial $\tau = 1$ slightly deeper, and at higher temperatures, in the hot component than in the cool component (where $\tau = 1$ is boosted in altitude by the COmospheric zone). At the limb, the inclined rays become optically thick at high altitudes in the COmosphere of the cool component, where it diverges markedly from the reference model. The pervasive cool zone now completely controls the spatial structure, effectively *shadowing* the hotter gas, suppressing the apparent $f_{\rm hot}$ below the already small value at disk center. The shadowing is moot for this scenario, however, because the cool component dominates the spatial average at all viewing angles.

Figure 11*b* depicts the center-to-limb behavior and off-limb extensions for Scenario Zero. Again, we can easily force good agreement between the simulations and observations of weak and strong $\Delta v = 1$ lines by adjusting the thermal structure of the cool component. A similar consideration applies to the predicted off-limb CO extensions through choice of the canopy altitude. The hot component plays only a minor role; it could be dispensed with entirely as far as the spatially averaged CO spectrum is concerned (although, of course, retention of a hot component would be politic vis-a-vis the UV diagnostics). Thus, Scenario Zero represents the situation in which the subcanopy COmosphere dominates what otherwise would be the low chromosphere, while the normal chromosphere resides in fine-scale structures of small filling factor. In the overlying canopy, however, the hot chromospheric gas might be more uniform and certainly more pervasive.

Figure 12 offers two variants of an alternative model in which the cool component is a minority constituent of the subcanopy zone but still can influence the limb spectrum of CO through geometrical shadowing. One realization of the scenario (Fig. 12*a*: *Scenario One*) has the cool component arrayed in the same fashion as the hot component of Scenario Zero (i.e., with $\Delta x_{\rm cool} = 1$ Mm; $f_{\rm cool} = 0.20$). Again,

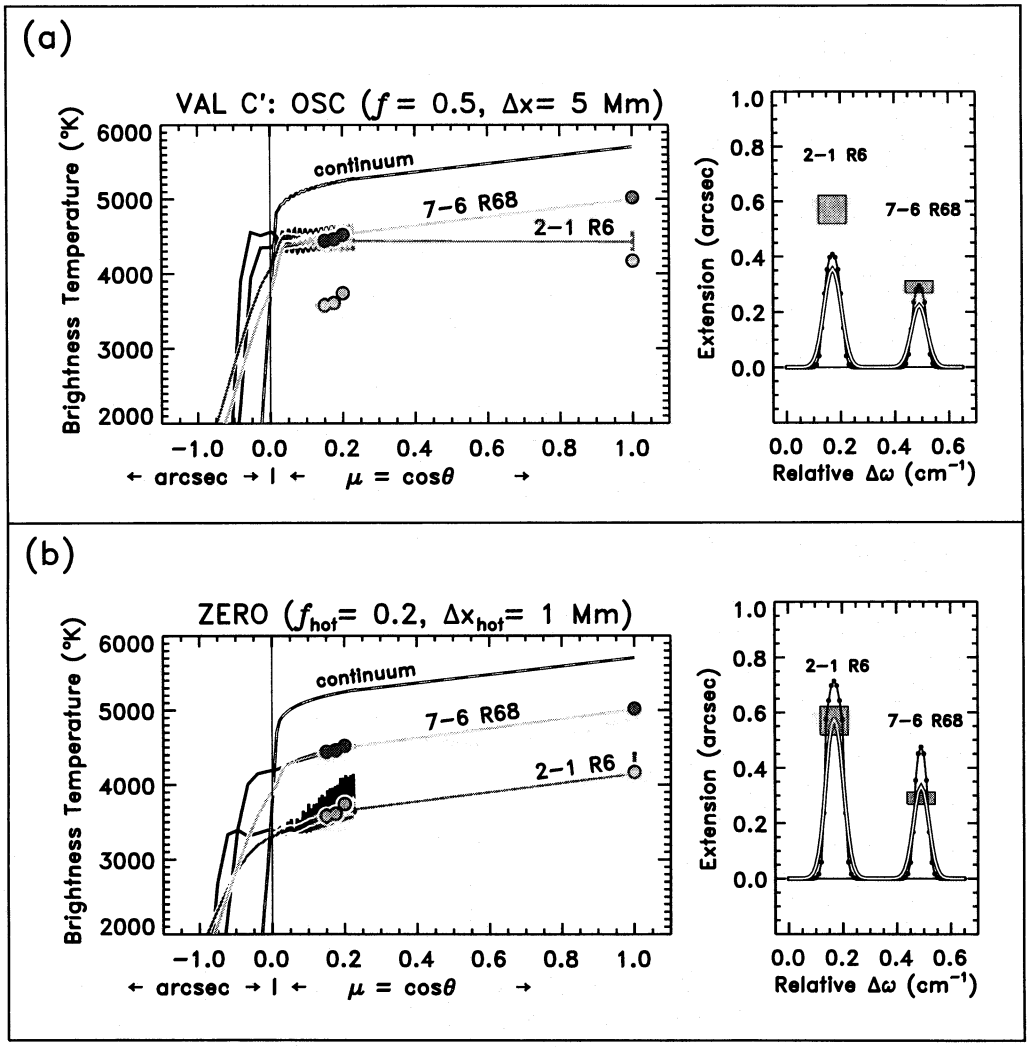

FIG. 11.—Same as Fig. 9 for (*a*) Model OSC and (*b*) Scenario Zero. The raggedness of the predicted spatial distributions for Scenario Zero reflects the range of values produced by the ensemble of inhomogeneous structures.

the properties of the cool component—minimum temperature, vertical thickness of cool region, and canopy height—were modified to match the spatially averaged behavior of the $\Delta v = 1$ lines at disk center and the limb. The $\mu = 1$ stigmatic spectrum shows the 20% coverage of cold dark points ($\Delta T \approx 2000$ K) required to shadow effectively the majority hot component at the extreme limb. Note that the radial thickness of the cool zone has increased with respect to Scenario Zero, and the minimum temperature has dropped by 500 K.

The companion Figure 13*a* indicates that Scenario One can match the empirical CO properties. Nevertheless, it also predicts high-contrast point-to-point thermal structure at disk center at a spatial resolution of 1″ (comparable to the best seeing-selected NIM frames, in light of the 0″.8 diffraction limit). Even at the limb, one should find significant thermal contrast at the 1″ scale. Such fluctuations are not seen in the best NIM strong-line maps. On that basis alone, we conclude that Scenario One is not viable. Furthermore, while the synthesized strong-line CO limb extension is 0″.6 at eclipse spatial resolution (and 75,000 resolving power with *no* scattered light), it declines to 0″.3 at the 1″ and 38,000 resolutions of our sharpest NIM frames. The weak-line extension is comparable to the 0″.25 predicted by VAL C′, again somewhat smaller than observed.

The best hope for the $f_{\rm cool} \ll 1$ scenario is to render the cool component as small as possible, so that it might escape detection at spatial resolutions no better than ≈1″. One cannot thin the structures without limit, however, because they still must be sufficiently opaque to "cast shadows" near the limb. For the 2–1 R6 transition, the transverse optical depth at line center is

$$\tau_0 = \kappa_0 \Delta x \approx 26[{\rm CO}]n_{15}\Delta x \;, \tag{1}$$

where Δx is the lateral size of the cool structure in Mm, $[{\rm CO}] \equiv n_{\rm CO}/(A_{\rm C}\, n_{\rm H})$ is the molecular concentration relative to the saturated limit (all carbon bound into CO), and n_{15} is the hydrogen density in units of 10^{15} cm^{-3}. In calculating κ_0, we assumed $T = 3000$ K, $\xi_t = 1.5$ km s^{-1}, and the line parameters of Goorvitch (1994). If we require the structures to be at least one optical depth thick, then

$$\Delta x \gtrsim 0.04 \times ([{\rm CO}]n_{15})^{-1}\ {\rm Mm}\;. \tag{2}$$

Generally, $n_{15} \approx 0.2$ at $h \approx -750$ km, near the middle of the COmospheric zone of the cool-component models. Thus, the opacity condition implies a minimum horizontal thickness of about 0.2 Mm or 0″.3. Higher CO densities could be attained if the cool zone were pushed deeper into the photosphere, below the $T_{\rm min}$ of VAL C′. However, then

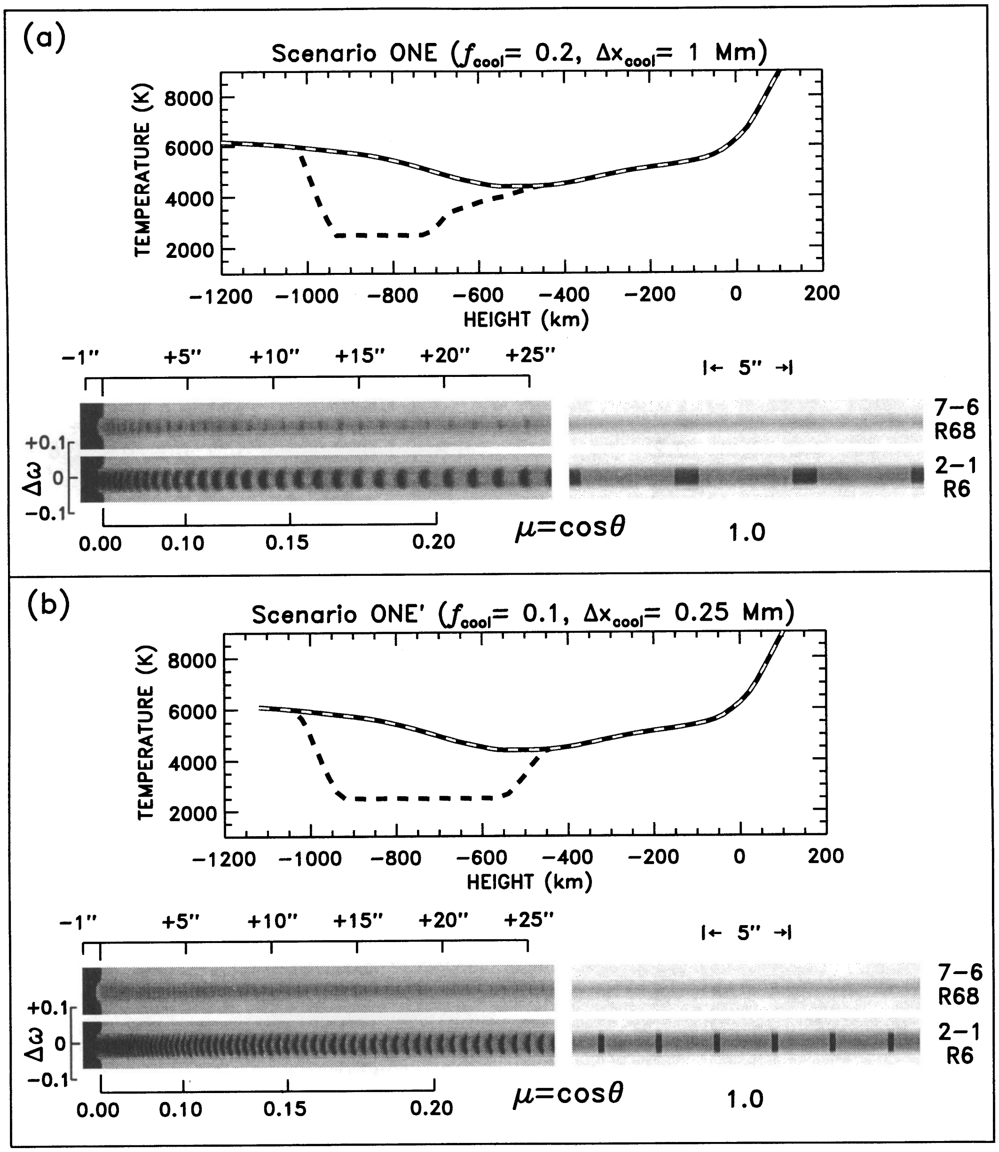

FIG. 12.—Same as Fig. 8, for small-scale cold structures embedded in a pervasive warm (VAL C′) atmosphere. (*a*) "Scenario One": covering fractions the reverse of Scenario Zero, i.e., 20% cool component (1 Mm width on 5 Mm centers) and 80% warm component and (*b*) "Scenario One′": small-scale cold component, 10% covering fraction in 0.25 Mm-wide structures.

the weak CO lines would be affected significantly. Furthermore, shadowing is most effective when the optically thick zone reaches *well above* $T_{\rm min}$ to maximize the projected length of the screening slab.

A second consideration places a limit on the minimum filling factor. The horizontal extent of the shadowed area is $\Delta z \tan\theta$, where Δz is the vertical thickness of the cool zone. Thus, the projected filling factor near the limb is

$$f_{\rm proj} = (\Delta x + \Delta z \tan\theta)/d\ , \qquad (3)$$

where d is the horizontal separation between the centers of the occulting structures. It follows (with $f_{\rm cool} \equiv \Delta x/d$) that

$$f_{\rm cool} = f_{\rm proj} \Big/ \left(1 + \frac{\Delta z}{\Delta x}\tan\theta\right) . \qquad (4)$$

The maximum likely brightness temperature contrast between the cool and hot components is about 2000 K, yielding a minimum temperature in the cool component of about 2500 K, the RE boundary temperature in the simulations of Anderson (1989). In order to duplicate the observed spatially averaged temperature deficit of about 1000 K at $\mu = 0.2$ (i.e., the "cool cores" of the CO lines near the limb), $f_{\rm proj}$ must be $\approx \frac{1}{2}$. If we take a minimum lateral size of 0.25 Mm and assume a radial thickness[3] comparable to the horizontal thickness, we find a minimum $f_{\rm cool} \approx 0.1$.

Scenario One′, in Figure 12*b*, embodies these limiting characteristics. In the companion Figure 13*b*, one sees that such fine-scale, sparsely distributed structures would be well hidden at best-NIM spatial resolution: the point-to-point thermal fluctuations are comparable only to those of the *p*-modes. However, the predicted off-limb extensions (at NIM spectral resolution) are much smaller than observed.

---

[3] Note that Δz refers specifically to that portion of a single cool structure that is optically thick for an inclined ray near the limb. The full vertical extent of the cool zone (i.e., the canopy altitude) is determined by the less restrictive condition of $\tau_{\rm total} \approx 1$ for an *off-limb* ray that can pass through *many* such structures (because the continuum is transparent and does not impose the natural truncation of the ray that occurs on the disk).

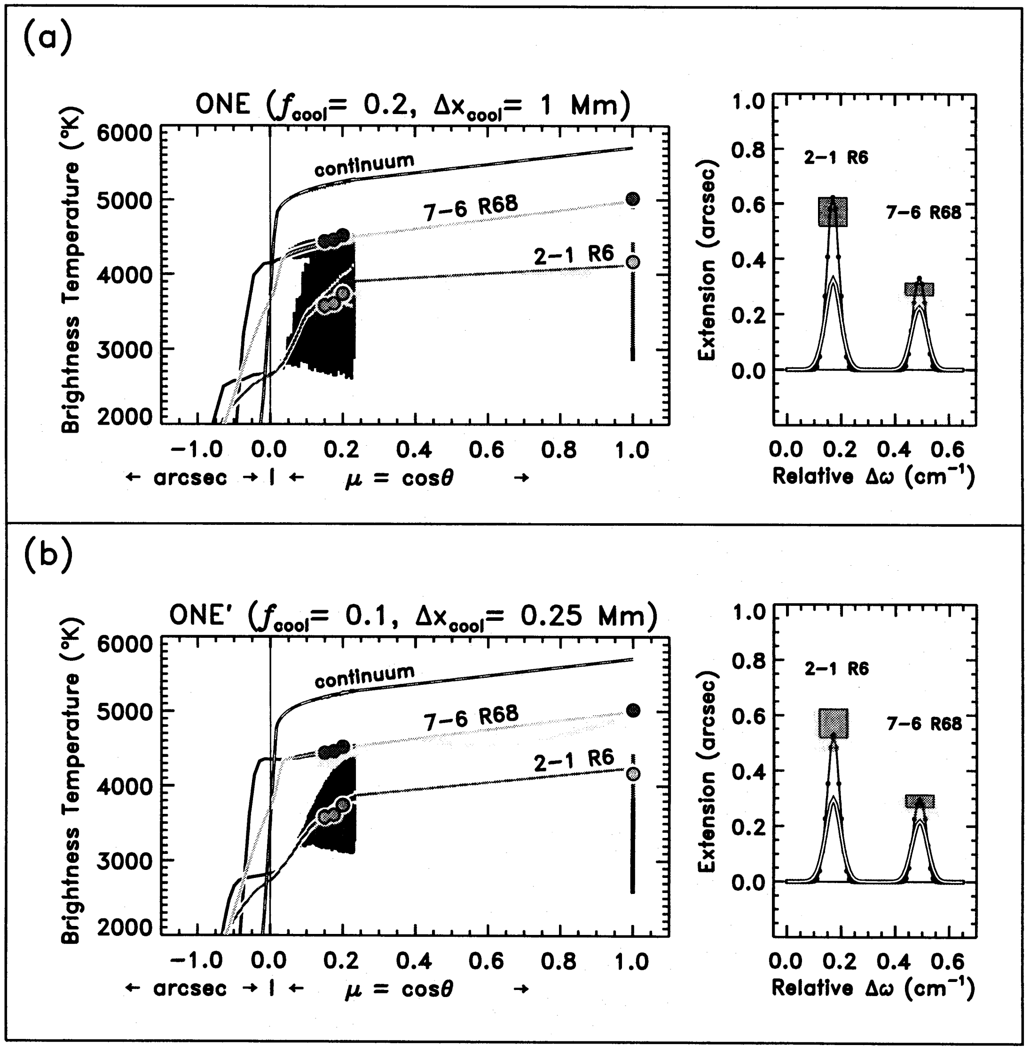

FIG. 13.—Same as Fig. 9 for (*a*) Scenario One and (*b*) Scenario One′. In the latter, the dark points are hidden at best-NIM spatial resolution but should be visible in optical molecular diagnostics (e.g., CN 388 nm and CH 430 nm). In addition, the predicted off-limb extensions at NIM spectral resolution are smaller than observed.

The off-limb extensions of the CO lines are sensitive to the filling fraction because the transverse optical depth is proportional to $L\langle n_{\rm CO}\rangle f_{\rm cool}$. Here, $L \approx 40$ Mm is the tangential sight line (transecting the shells between $h = -800$ km and $T_{\rm min}$), $\langle n_{\rm CO}\rangle$ is the average CO density, and we have assumed that the hot component contributes nothing. Accordingly, the off-limb extensions are maximum for the $f_{\rm cool} \approx 1$ models and naturally decrease for the $f_{\rm cool} \ll 1$ scenarios.

Furthermore, while any fine-scale dark structures would have relatively low contrast even in diffraction-limited mid-IR maps, one might find a stronger signature in, for example, CN 388 nm filtergrams taken under conditions of good seeing. Existing CN pictures reveal an obvious fine-scale $f \ll 1$ sprinkling of *bright points* associated with the supergranulation network and cell-interior $\rm K_{2V}$ events (Sheeley 1969; Fig. 2 above); but an equivalent pattern of dark points, to our knowledge, is not seen. Similarly, 0.″2 resolution *G*-band filtergrams from the Swedish Solar Telescope on La Palma show a sparse distribution of fine-scale bright points but no hint of a corresponding population of cold dark elements (Berger et al. 1995). Thus, the body of evidence weighs against the $f_{\rm cool} \ll 1$ scenarios.

5. CHEMICAL DYNAMICS AND CO COOLING TIMESCALES

We now address a final subject, namely the formation and destruction of the CO molecules high in the solar photosphere and the resulting influence on the radiative cooling timescales. The issue has been considered in a number of previous studies, not only in the context of stellar atmospheres (Muchmore & Ulmschneider 1985; Muchmore et al. 1987; Cuntz & Muchmore 1994) and circumstellar envelopes (Mamon, Glassgold, & Huggins 1988; Beck et al. 1992; Spaans et al. 1994) but also in environments ranging from dense interstellar clouds (Herbst & Klemperer 1973; Glassgold & Langer 1976; Gredel, Lepp, & Dalgarno 1987; Neufeld & Dalgarno 1989; Neufeld & Kaufman 1993) to the metal-rich ejecta of supernovae (Petuchowski et al. 1989; Dalgarno, Du, & You 1990; Rawlings & Williams 1990).

The formation, destruction, and radiative cooling timescales of CO play crucial roles in understanding how the thermal bifurcation comes about, given the frequent hydrodynamical disruptions of the solar outer photosphere by the cell-interior $\rm K_{2V}$ "flashes" (e.g., Rutten & Uitenbroek 1991). The heating events are found only over about 10% of the surface at any one time, but the durations are such that a given location in a supergranule interior probably is affected at least once or twice per hour. If the CO in the COmospheric portion of the bright point were completely dissociated, then a long reformation time would guarantee that the CO constantly would be out of chemical equilibrium, and the autocatalytic molecular cooling might never have the opportunity to restore low, near-RE temperatures.

Usually the most favored mechanism to produce diatomic molecules is a three-body collision, in which the extra partner is available to carry off the heat of formation. The rate depends on density *cubed*, however, and the reaction is quite slow in the tenuous outer layers of even high-gravity dwarf stars like the Sun. Direct radiative association

$$C + O \rightarrow CO + h\nu\ , \qquad (5)$$

is much more important than 3-body reactions at low density but still has a very small rate coefficient (Dalgarno et al. 1990). If the main destruction path is collisional dissociation

$$CO + H \rightarrow C + O + H\ , \qquad (6)$$

then the formation rate in a neutral gas is

$$\dot{n}_{CO} \approx k_{ra}(1 - [CO]) - k_{cd}[CO]\ \mathrm{cm}^{-3}\ \mathrm{s}^{-1}\ , \qquad (7)$$

where the *k*'s are the rate coefficients (in units commensurate with the CO concentration defined previously), and the factor (1 − [CO]) accounts for the depletion of atomic carbon (the analogous factor for oxygen is less important because $A_O \approx 2 \times A_C$). Equation (7) can be recast in terms of the concentration

$$[\dot{CO}] \approx \tilde{k}_1 - \tilde{k}_{-1}[CO]\ \mathrm{s}^{-1}\ , \qquad (8)$$

which has the solution

$$[CO] \approx (\tilde{k}_1/\tilde{k}_{-1}) \times (1 - e^{-k_{-1}t})\ , \qquad (9)$$

and associated timescale

$$t_{CO}^{chem} \approx (\tilde{k}_{-1})^{-1}\ \mathrm{s}\ , \qquad (10)$$

(see, e.g., Herbst & Klemperer 1973). With the definitions and abundances summarized in Table 1 and the reaction coefficients of Table 2, the equilibrium concentration of CO could be as much as

$$[CO] \approx (1 + 40 \times \bar{T}^{22.2})^{-1} \approx 0.8 \quad (T = 4000\ \mathrm{K})\ , \qquad (11)$$

where $\bar{T} \equiv T/(5000\ \mathrm{K})$. Depending on temperature and density, the formation time might be as long as

$$t_{CO}^{chem} \approx 4 \times 10^4 \frac{\bar{T}^{-0.6}}{(1 + 40 \times \bar{T}^{22.2})} n_{15}^{-1}\ \mathrm{s}\ , \qquad (12)$$

which is about 10 hr for $T = 4000$ K at altitudes where $n_{15} \approx 1$ (i.e., near the VAL C′ $T_{\min}$), much longer than either typical radiative cooling times (a few minutes) or dynamical timescales (a sonic flow can traverse a pressure scale height in 10–15 s). In the extended envelopes of red giant stars, t_{CO}^{chem} can approach months or even years (e.g., Cuntz & Muchmore 1994). (Note, however, that the formation time at $T = 5000$ K is 40 times shorter, primarily because the final concentration is much reduced from its near-saturated value at 4000 K).

TABLE 1

DEFINITIONS

Auxiliary Quantities	Normalized Concentrations
$\bar{T} \equiv T/(5000\ \mathrm{K})$	$[O] \equiv n_O/A_O n_H \approx 1 - \frac{1}{2}[CO]$
$n_{15} \equiv n_H/(10^{15}\ \mathrm{cm}^{-3})$	$[C] \equiv n_C/A_C n_H \approx 1 - [CO]$
$A_H \equiv 1$	$[H_2] \equiv n_{H_2}/10^{-4} n_H$
$A_{He} \equiv 0.1$	$[OH] \equiv n_{OH}/10^{-8} n_H$
$A_O \equiv 8 \times 10^{-4}$	$[CO] \equiv n_{CO}/A_C n_H$
$A_C \equiv 4 \times 10^{-4}$	$[He^+] \equiv n_{He^+}/10^{-8} n_H$

However, such t_{CO}^{chem} estimates—based on direct radiative associations balanced by collisional dissociations—ignore other chemical paths that might be more effective. The following discussion is based on developments described in a series of papers concerning the formation of molecules in strong neutral winds from young stellar objects (Glassgold, Mamon, & Huggins 1989; Ruden, Glassgold, & Shu 1990; Glassgold, Mamon, & Huggins 1991). There, conditions of temperature and density approximate those at the base of the solar chromosphere/COmosphere.

In particular, the species-exchange reaction,

$$C + OH \rightarrow CO + H\ , \qquad (13)$$

has a large rate coefficient and dominates the formation of CO when the OH concentration has attained typical values of $[OH] \equiv n_{OH}/(10^{-8} n_H) \approx 1$ or more. The OH equilibrates more rapidly than the CO owing to its much smaller final concentration and to the fast reaction

$$O + H_2 \rightarrow OH + H\ , \qquad (14)$$

which has an energy barrier of only 4500 K (Millar et al. 1991). A reservoir of H_2 is maintained by ternary association

$$3H \rightarrow H_2 + H\ , \qquad (15)$$

which is effective even at low density owing to the large abundance of atomic hydrogen. The equilibrium concentration of H_2—arising solely from a balance between ternary associations and collisional dissociations (the dominant loss)—can be as large as

$$[H_2] \equiv n_{H_2}/(10^{-4} n_H) \approx 0.15\bar{T}^{-10.6} n_{15}\ . \qquad (16)$$

Together with the destruction mechanism

$$CO + H \rightarrow OH + C\ , \qquad (17)$$

the OH pathway leads to a CO formation timescale of about

$$t_{CO}^{chem} \approx 0.5\bar{T}^{-16.2} n_{15}^{-1}\ \mathrm{s}, \qquad (18)$$

which is only 20 s at $T \approx 4000$ K and $n_{15} \approx 1$. Again, the timescale decreases rapidly with increasing temperature owing primarily to the smaller final concentration of the molecules.

Furthermore, if there is a significant overionization of atomic carbon—for example by H I Lyα irradiation—then the molecular ion CO^+ can be produced by a fast reaction of C^+ with OH

$$C^+ + OH \rightarrow CO^+ + H\ , \qquad (19)$$

where again a short equilibration time follows from the small final concentration of the species and the rapid formation rate. The CO^+ is an important source of CO through the charge-exchange reaction

$$CO^+ + H \rightarrow CO + H^+\ . \qquad (20)$$

1996ApJ...460.1042A

TABLE 2

HIGH-TEMPERATURE H_2–OH–CO CHEMISTRY

NUMBER	REACTION	RATE COEFFICIENT ($T \approx 5000$ K)	RATIONALIZED RATE ($\mathrm{cm^{-3}\ s^{-1}}$)	REFERENCES
Radiative Association ($\mathrm{cm^3\ s^{-1}}$)				
(1)…….	$O + H \rightarrow OH + h\nu$	$3 \times 10^{-19} \bar{T}^{-0.4}$	$2 \times 10^{8} \bar{T}^{-0.4} [O] n_{15}^2$	UMIST
(2)…….	$C + O \rightarrow CO + h\nu$	$3 \times 10^{-17} \bar{T}^{0.6}$	$1 \times 10^{7} \bar{T}^{0.6} [C][O] n_{15}^2$	DDY90
3-Body Association ($\mathrm{cm^6\ s^{-1}}$)				
(3)…….	$3H \rightarrow H_2 + H$	$6 \times 10^{-33} \bar{T}^{-4.0}$	$6 \times 10^{12} \bar{T}^{-4.0} n_{15}^3$	BDDG72
(4)…….	$O + 2H \rightarrow OH + H$	$\approx 1 \times 10^{-32}$	$\approx 8 \times 10^{9} [O] n_{15}^3$	BDDG72
(5)…….	$C + O + H \rightarrow CO + H$	$2 \times 10^{-33} \bar{T}^{-3.5}$	$6 \times 10^{5} \bar{T}^{-3.5} [C][O] n_{15}^3$	BDDG76[a]
Species Exchange ($\mathrm{cm^3\ s^{-1}}$)				
(6)…….	$H_2 + O \rightarrow OH + H$	$6 \times 10^{-11} \bar{T}^{1.9}$	$5 \times 10^{12} \bar{T}^{1.9} [H_2][O] n_{15}^2$	UMIST
(7)…….	$OH + H \rightarrow H_2 + O$	$4 \times 10^{-11} \bar{T}^{1.7}$	$4 \times 10^{11} \bar{T}^{1.7} [OH] n_{15}^2$	UMIST
(8)…….	$OH + C \rightarrow CO + H$	$5 \times 10^{-10} \bar{T}^{0.5}$	$2 \times 10^{9} \bar{T}^{0.5} [OH][C] n_{15}^2$	UMIST
(9)…….	$CO + H \rightarrow OH + C$	$2 \times 10^{-15} \bar{T}^{16.2}$	$8 \times 10^{11} \bar{T}^{16.2} [CO] n_{15}^2$	From (8)[b]
Collisional Dissociation ($\mathrm{cm^3\ s^{-1}}$)				
(10)……	$H_2 + H \rightarrow 3H$	$4 \times 10^{-13} \bar{T}^{6.6}$	$4 \times 10^{13} \bar{T}^{6.6} [H_2] n_{15}^2$	BDDG72
(11)……	$OH + H \rightarrow O + 2H$	$2 \times 10^{-13} \bar{T}^{10.4}$	$2 \times 10^{9} \bar{T}^{10.4} [OH] n_{15}^2$	UMIST
(12)……	$CO + H \rightarrow C + O + H$	$1 \times 10^{-18} \bar{T}^{22.8}$	$4 \times 10^{8} \bar{T}^{22.8} [CO] n_{15}^2$	BDDG76
Dissociative Charge Exchange ($\mathrm{cm^3\ s^{-1}}$)				
(13)……	$CO + He^+ \rightarrow C^+ + O + He$	2×10^{-9}	$8 \times 10^{9} [CO][He^+] n_{15}^2$	UMIST

[a] Rate for $C + O + Ar \rightarrow CO + Ar$, assumed to be similar for $Ar \rightarrow H$.

[b] By detailed balance.

REFERENCES.—UMIST: Millar et al. 1991; DDY90: Dalgarno, Du, & You 1990; BDDG72: Baulch et al. 1972; BDDG76: Baulch et al. 1976.

Another formation channel via CH,

$$C + H_2 \rightarrow CH + H \,, \tag{21}$$

$$O + CH \rightarrow CO + H \,, \tag{22}$$

is less favored than the OH pathway owing to the higher energy barrier of the first reaction (14,100 K: Millar et al. 1991).

In addition to the loss mechanisms described previously, CO can be degraded by charge exchange

$$CO + H^+ \rightarrow CO^+ + H \tag{23}$$

and—when a significant population of ionized helium is present—by dissociative charge exchange

$$CO + He^+ \rightarrow C^+ + O + He \,. \tag{24}$$

Far-UV photodissociation and destruction by cosmic-ray particles—crucial in the interstellar medium and in diffuse clouds (e.g., van Dishoeck 1988)—are much less important in the low chromosphere because of shielding by the large overlying columns of atomic hydrogen and carbon. The collisional destruction channels are very sensitive to temperature owing to the high dissociation potential of CO (11.1 eV). The destruction timescale for CO based on the chemical exchange reaction (eq. [17]) is the same as the formation timescale given in equation (18), much less than 1 s at $T \approx 6000$ K and $n_{15} \approx 1$. Thus, a transiently heated volume of COmosphere could be completely cleansed of molecules. When the heating is suspended, however, the gas will cool radiatively to the H^- equilibrium temperature of about 4900 K on a timescale of minutes, and CO molecules will begin to form again via the OH pathway. Once even a small concentration of CO is present, CO cooling can commence and further chill the gas below the H^- plateau temperature.

The (LTE) H^- cooling timescale can be estimated as follows:

$$t_{H^-}^{\mathrm{rad}} = \frac{\frac{3}{2} n_H k (T - T_E)}{4\pi \bar{\kappa}_{H^-} \sigma (T^4 - T_E^4)} \tag{25}$$

$$\approx 1.2 [e]^{-1} n_{15}^{-1} \bar{T}^{-2} \text{ minutes} \,, \tag{26}$$

where $T_E \approx (\frac{1}{2})^{1/4} T_{\mathrm{eff}}$ is the H^- equilibrium temperature, $[e] \equiv n_e/(10^{-4} n_H)$ is the electron concentration relative to its low-temperature limit (see Ayres 1979), and σ is the Stefan-Boltzmann constant. We have assumed that the H^- is optically thin in the high photosphere and that the background radiation field can be approximated by a Planckian with $T_R \approx T_{\mathrm{eff}}$ and a geometrical dilution of $w = \frac{1}{2}$. The Planck-mean opacity (for b–f and f–f transitions) is $\bar{\kappa}_{H^-} \approx 8 \times 10^{-12} [e] n_{15}^2 \bar{T}^{-1}\ \mathrm{cm^{-1}}$. Equation (26) follows when the temperature is close to T_E (NH give a similar relationship without the factor π in the denominator). Thus the H^- cooling timescale is only minutes at the top of the photosphere ($n_{15} \approx 1$).

The CO radiative cooling timescale can be estimated similarly. The CO cooling function is given by

$$\Lambda_{CO} \approx \sum_{v=1}^{\infty} hc\omega_{vv-1} (A_{vv-1} n_v + B_{vv-1} n_v \bar{J}_{v-1v} - B_{v-1v} n_{v-1} \bar{J}_{v-1v}) \tag{27}$$

$$\approx hc\bar{\omega} \bar{A} n_{CO} \times \left(1 - \frac{1}{2} \frac{e^{\omega_0/T} - 1}{e^{\omega_0/T_R} - 1}\right) , \tag{28}$$

where A_{vv-1} is the spontaneous decay rate from upper vibrational level v in the fundamental (band) transition $v \rightarrow v-1$; the Bs are the stimulated emission and induced absorption coefficients, respectively, operating on the profile-average mean intensity $\bar{J}$; n_v is the population of the vibrational level; and $hc\omega_{vv-1}$ is the mean photon energy. The second line is obtained by taking $\bar{J} \approx \frac{1}{2}\mathscr{B}_\omega(T_R)$, where $\mathscr{B}_\omega$ is the Planck function and T_R is a radiation temperature parameterizing the mean intensity for dilution factor $w = \frac{1}{2}$, and noting that $n_{v-1}/n_v \approx e^{\omega_0/T}$, where $\omega_0 \approx 3120$ K represents the vibrational spacing in the ground electronic state of the CO molecule. For temperatures close to the equilibrium temperature T_E, where the second term in the parentheses of equation (28) is unity, it is convenient to express the cooling rate in terms of $(1 - T_E/T)$, analogous to the factor appearing in the H^- radiative balance. Note that the equilibrium temperature for CO will be much smaller than for H^- because the equivalent profile-average Planckian intensity in the CO cores ($T_R \approx 4500$ K) is much lower than the $T_{\rm eff} = 5770$ K appropriate for H^- and because the balance is accomplished with *monochromatic* thermal emission $\mathscr{B} \sim T$ (the CO bands are concentrated in the mid-IR), rather than with the integrated Planckian $\mathscr{B} \sim T^4$ appropriate to the broadband H^- opacity. In practice, the CO equilibrium temperature is $T_E \approx 2800$ K, similar to the RE value in the simulations of Anderson (1989). In equation (28), $\bar{A} \equiv \sum_{v=1}^{\infty} A_{vv-1}\, n_v / \sum_{v=0}^{\infty} n_v \approx 35\ {\rm s}^{-1}$, based on the spontaneous decay rates tabulated by Radzig & Smirnov (1985). Note that spontaneous decays are not possible from the ground vibrational state $v = 0$ and that the sum over the vibrational level populations is essentially the CO abundance (virtually all of the molecules are in the ground electronic state). The CO cooling for $T \approx T_E$ can be approximated as

$$\Lambda_{\rm CO} \approx 10[{\rm CO}]n_{15} \times (1 - T_E/T)\ {\rm ergs\ cm^{-3}\ s^{-1}}\ , \quad (29)$$

and the associated timescale is

$$t_{\rm CO}^{\rm rad} = \frac{\frac{3}{2}n_{\rm H}k(T - T_E)}{\Lambda_{\rm CO}} \quad (30)$$

$$\approx 1.7[{\rm CO}]^{-1}\bar{T}\ {\rm minutes}\ , \quad (31)$$

which is comparable to the H^- cooling time at $n_{15} \approx 1$ for a saturated abundance of CO. The cooling timescale is *shorter* than the formation time at 3000 K but longer than the chemical timescale for $T \gtrsim 4000$ K. However, the $\Delta v = 1$ cooling time (for a saturated CO abundance) is *independent of density*, unlike the H^- cooling and the CO chemical formation timescales, both of which increase with decreasing density. Detailed NLTE calculations for model COOLC verify the estimate given above and the density insensitivity.

On the other hand, in a gas cooling from the H^- equilibrium temperature of $\approx$4900 K, the CO abundance is far below saturation, and the steep temperature dependence of the CO concentration must be taken into account when calculating the cooling time. In the high-temperature limit (4000 K $\lesssim T \lesssim$ 5000 K),

$$[{\rm CO}] \approx 5 \times 10^{-3}\bar{T}^{-26.1}n_{15}\ . \quad (32)$$

The time rate of change of the temperature, assuming only the CO cooling, is

$$\dot{T} \approx \frac{-\Lambda_{\rm CO}}{\frac{3}{2}n_{\rm H}k}\ {\rm K\ s^{-1}}\ . \quad (33)$$

The time to cool from temperature T_1 to a lower temperature T_0 is the integral of the inverse of that expression. Taking a high-temperature approximation to the cooling function

$$\Lambda_{\rm CO} \approx 3.5\bar{T}^{1.4}n_{15}[{\rm CO}]\ {\rm ergs\ cm^{-3}\ s^{-1}}\ , \quad (34)$$

with the equation (32) expression for [CO] and performing the indicated integration, we find

$$t_{\rm CO}^{\rm rad} \approx 37\bar{T}_1^{25.7}n_{15}^{-1}\ {\rm minutes}\ , \quad (35)$$

for any $T_0 < 4500$ K. Thus, the return to cool plasma conditions is limited mostly by the relatively slow CO cooling time in the high-temperature regime (where the CO concentration is unsaturated). The steep temperature dependence reflects the autocatalytic character of the CO cooling.

In this regard, stars as hot as or hotter than the Sun represent the worst possible case for the operation of the autocatalytic molecular cooling: the H^- equilibrium temperature—to which a previously hot gas in the outer photosphere naturally returns when the supraradiative (i.e., mechanical) heating is interrupted—is about 1000 K hotter than the regime in which molecular processes are most efficient. However, if other sources of cooling are effective at $T \approx T_E^{H^-}$, say the iron "haze" described by Anderson (1989), the overall cooling timescale will be shorter than the estimate given above. At lower temperatures, the (equilibrium) CO radiative cooling times are short. The chemical formation times are long, however, owing to the slowing of the destruction rates which in turn yields a large, saturated final abundance of CO. Nevertheless, once the chemistry has proceeded to equilibrium, the CO cooling timescale is independent of density, an important consideration given that other cooling timescales—ultimately deriving from collisional processes—will depend inversely on the density (as CO does in the high-temperature regime). Thus, once a cool zone has been established, it should strongly resist changes in its thermal state.

The fact that the CO cooling—and hence the thermal bifurcation mechanism—depends on density no worse than inversely is of greater significance for giant stars than for dwarfs like the Sun. To see that, we write the timescale for the onset of effective CO cooling as (see eq. [18] or eq. [35])

$$t_{\rm CO} \sim n_{15}^{-1}\ . \quad (36)$$

In giant stars the atmospheric densities are much lower than in dwarfs, greatly lengthening the timescale. According to arguments given by Ayres (1979), the mass column density (m: g cm^{-2}) high in the stellar photosphere scales roughly as

$$m \sim g^{-1/2}\ , \quad (37)$$

where g is the surface gravity. (The relationship devolves from the pressure-squared sensitivity of H^- formation). The hydrostatic gas pressure is $P \approx n_{\rm H}kT \approx gm$. Thus, the gas density at that level scales roughly as

$$n_{\rm H} \sim g^{1/2}\ , \quad (38)$$

and the cooling timescale varies as

$$t_{\rm CO} \sim g^{-1/2}\ . \quad (39)$$

In other words, the CO cooling timescale increases with decreasing surface gravity, but only as the square root. In contrast, hydrodynamical timescales

$$t_{\rm hydro} \approx H/c_s \sim g^{-1}\ , \quad (40)$$

where H is the scale height (which depends inversely on g) and c_s is the sound speed (independent of density). Thus, the hydrodynamical timescales on giants are stretched correspondingly more than chemical timescales, compared with their relative behavior on the high-gravity dwarfs. To the extent that thermal bifurcation effects are important in dwarf stars like the Sun, they should be even more significant in late-type giants.

To complete the discussion of chemical and radiative timescales, we mention a hybrid timescale that might be relevant in some situations (Ayres 1991). In particular, it might not be necessary to achieve the full equilibrium concentration of CO in order for the $\Delta v = 1$ cooling to reach peak efficiency. Because the LTE CO cooling maximizes when the strong lines of the bands are *translucent* ($0.3 \lesssim \tau \lesssim 1$), a significant timescale is that required to achieve $\tau \gtrsim 0.5$. Given the strong-line opacity cited in equation (1), above, we can estimate the radial optical depth by substituting the density scale height, $H \approx 0.070$ Mm, for Δx to obtain

$$\tau_{\rm CO} \approx 1.7[{\rm CO}]n_{15} . \qquad (41)$$

Thus, the timescale to produce enough CO to ensure maximum radiative cooling, $[{\rm CO}] \gtrsim 0.3$ at $n_{15} \approx 1$, can be *several times faster* than the timescale to achieve the equilibrium concentration (i.e., $[{\rm CO}] \approx 1$ at temperatures low enough that all of the carbon associates into CO). Using the gravity scalings, above, one sees that the optical depth will be enhanced on giant stars by the factor $g^{-1/2}$, thereby potentially increasing the importance of the hybrid timescale and further widening the disparity between the hydrodynamical and CO cooling times.

6. SUMMARY AND DISCUSSION

Stigmatic imaging of the CO fundamental bands with the NIM has opened a new chapter in the study of the high-altitude layers of the solar atmosphere beneath the chromospheric "canopy." The recent work by us and others has shown that the spatially resolved thermal and velocity fluctuations of the outer photosphere are strongly connected to the p-mode interference pattern, aside from a sparse population of long-lived bright points associated with the CaK network and rare "cooling" events of unknown origin. Yet, the amplitudes of the oscillations in the high layers are modest when compared with the chaotic dynamics of the deep photosphere driven by the subsurface convection zone. Given that the chromosphere is thought to be heated at least partly by acoustic energy deposition, it is remarkable that the CO layers show so little evidence for disruption by large-amplitude velocity disturbances.

On the one hand, it is tempting to propose that the spatial resolution of the existing stigmatic imagery still is not sufficient to resolve the acoustic wave field, a possibility supported by the fact that the FTS-measured nonthermal line widths of CO greatly exceed the rms velocity amplitudes of the resolved p-modes. On the other hand, the present work suggests a different explanation: relatively little acoustic energy is deposited in the layers historically associated with the initial chromospheric temperature inversion. Our numerical simulations favor a scenario in which most of the atmosphere below the base of the magnetic canopy (at a height of 900 km above $\tau_{500\,{\rm nm}} = 1$) is a thermally depressed *COmosphere*, substantially cooler than the $T_{\rm min}$ of popular models. Perhaps significantly, the recent numerical simulations by CS of acoustic wave propagation in the solar atmosphere predict a mean shock formation height closer to the base of the canopy (350 km *above* $T_{\rm min}$) than to the lower lying temperature minimum itself.

Finally, we have argued that multistep chemical reactions, rather than direct radiative associations, control the formation of CO in the COmosphere. Under these circumstances, the chemical reaction and radiative cooling rates probably are sufficiently fast to maintain a quasi-equilibrium cool zone in spite of occasional disruptions by K_{2V} heating events (if the disturbances truly are capable of imposing sharp, dissociating temperature spikes in the COmosphere).

7. FOR THE FUTURE

The next step in the exploration of the solar COmosphere is to coordinate more explicitly imaging sequences in CO and signatures of the hotter gas like CaK and Hα. Such an experiment was conducted during a recent NIM/CO run in 1995 May and will be the subject of the next paper in this series.

The performance of the instrument itself can be improved significantly by utilizing the double-pass capability of the spectrograph: increased spectral resolution is essential to many of the observational projects envisioned for the future. Equally important is the development of high-resolution IR spectrographs for nighttime work. Instruments like the NOAO Phoenix will soon open new windows onto the operation of thermal bifurcation in the stars. At the same time, more detailed studies of the CO chemistry and cooling—particularly in a time-dependent hydrodynamical setting—are needed in order to predict fully the response of the COmosphere to transient heating. The stellar work, in turn, will help clarify the thermal regulation of the many other cosmic environments nurtured by the autocatalytic formation of molecules.

We are grateful to D. Jaksha and C. Plymate for providing technical assistance. This work was supported by grant AST-92 18063 from the National Science Foundation to the University of Colorado.

REFERENCES

Anderson, L. S. 1989, ApJ, 339, 558
Anderson, L. S., & Athay, R. G. 1989, ApJ, 346, 1010
Avrett, E. H. 1995, in Infrared Tools for Solar Astrophysics: What's Next?, ed. J. Kuhn & M. Penn (Singapore: World Scientific), 303
Ayres, T. R. 1975, ApJ, 201, 799
———. 1979, ApJ, 228, 509
———. 1981, ApJ, 244, 1064
———. 1991, in Mechanisms of Chromospheric and Coronal Heating, ed. P. Ulmschneider, E. R. Priest, & R. Rosner (New York: Springer), 228
Ayres, T. R., & Brault, J. W. 1990, ApJ, 363, 705 (AB)
Ayres, T. R., & Linsky, J. L. 1976, ApJ, 205, 874
Ayres, T. R., & Testerman, L. 1981, ApJ, 245, 1124 (AT)
Ayres, T. R., & Wiedemann, G. R. 1989, ApJ, 338, 1033 (AW)
Baulch, D. L., Drysdale, D. D., Duxbury, J., & Grant, S. 1972, Evaluated Kinetic Data for High Temperature Reactions, Vol. 1 (London: Butterworth's)
———. 1976, Evaluated Kinetic Data for High Temperature Reactions, Vol. 3 (London: Butterworth's)
Beck, H. K. B., Gail, H.-P., Henkel, R., & Sedlmayr, E. 1992, A&A, 265, 626
Beckers, J. M., & Artzner, G. 1974, Sol. Phys., 37, 309
Berger, T., Shine, R., Tarbell, T., Title, A., & Scharmer, G. 1995, BAAS, 26, 1465

Brault, J. W. 1979, Oss. Mem. Arcetri, 106, 33
Carlsson, M., & Stein, R. F. 1994, in Chromospheric Dynamics, ed. M. Carlsson (Oslo: Inst. of Theoretical Astrophysics), 79 (CS)
Clark, T. A., Lindsey, C. A., Rabin, D. M., & Livingston, W. C. 1995, in Infrared Tools for Solar Astrophysics: What's Next?, ed. J. Kuhn & M. Penn (Singapore: World Scientific), 133
Cuntz, M., & Muchmore, D. O. 1994, ApJ, 433, 303
Dalgarno, A., Du, M. L., & You, J. H. 1990, ApJ, 349, 675
Farmer, C. B., & Norton, R. H. 1989, A High-Resolution Atlas of the Infrared Spectrum of the Sun and Earth Atmosphere from Space, Vol. 1: The Sun (NASA RP-1224) (Washington: NASA)
Glassgold, A. E., & Langer, W. D. 1976, ApJ, 204, 403
Glassgold, A. E., Mamon, G. A., & Huggins, P. J. 1989, ApJ, 336, L29
———. 1991, ApJ, 373, 254
Goorvitch, D. 1994, ApJS, 95, 535
Gredel, R., Lepp, S., & Dalgarno, A. 1987, ApJ, 323, L137
Grevesse, N., Lambert, D. L., Sauval, A. J., van Dishoeck, E. F., Farmer, C. B., & Norton, R. H. 1991, A&A, 242, 488
Herbst, E., & Klemperer, W. 1973, ApJ, 185, 505
Holweger, H., & Müller, E. A. 1974, Sol. Phys., 39, 19
Komm, R., Mattig, W., & Nesis, A. 1990, A&A, 239, 340
Linsky, J. L. 1968, Ph.D. thesis, Harvard University; also released as SAO Spec. Rept. No. 274
Lites, B. 1994, in Chromospheric Dynamics, ed. M. Carlsson (Oslo: Inst. of Theoretical Astrophysics), 1
Livingston, W., & Wallace, L. 1991, An Atlas of the Solar Spectrum in the Infrared from 1850 to 9000 cm^{-1} (1.1 to 5.4 μm) (NSO Tech. Rept. No. 91-001) (Tucson: National Solar Observatory)
Maltby, P., Avrett, E. H., Carlsson, M., Kjeldseth-Moe, O., Kurucz, R. L., & Loeser, R. 1986, ApJ, 306, 284 (MACKKL)
Mamon, G. A., Glassgold, A. E., & Huggins, P. J. 1988, ApJ, 328, 797
Mauas, J., Avrett, E. H., & Loeser R. 1990 ApJ, 357, 279
Millar, T. J., Rawlings, J. M. C., Bennett, A., Brown, P. D., & Charnley, S. B. 1991, A&AS, 87, 585
Muchmore, D., Nuth, J., & Stencel, R. 1987, ApJ, 315, L141
Muchmore, D., & Ulmschneider, P. 1985, A&A, 142, 393
Neufeld, D. A., & Dalgarno, A. 1989, ApJ, 340, 869
Neufeld, D. A., & Kaufman, M. J. 1993, ApJ, 418, 263
Noyes, R. W., & Hall, D. N. B. 1972a, BAAS, 4, 389
———. 1972b, ApJ, 176, L89
Petuchowski, S. J., Dwek, E., Allen, J. E., Jr., & Nuth, J. A., III. 1989, ApJ, 342, 406
Rabin, D. M. 1994, in IAU Symp. 154, Infrared Solar Physics, ed. D. M. Rabin, J. T. Jefferies, & C. Lindsey (Dordrecht: Kluwer), 449
Radzig, A. A., & Smirnov, B. M. 1985, Reference Data on Atoms, Molecules, and Ions (New York: Springer)
Rawlings, J. M. C., & Williams, D. A. 1990, MNRAS, 246, 208
Ruden, S. P., Glassgold, A. E., & Shu, F. H. 1990, ApJ, 361, 546
Rutten, R. J., & Uitenbroek, H. 1991, Sol. Phys., 134, 15
Sheeley, N. R. 1969, Sol. Phys., 9, 347
Solanki, S. K., Livingston, W., & Ayres, T. 1994, Science, 263, 64 (SLA)
Spaans, M., Tielens, A., van Dishoeck, E., & Bakes, E. 1994, ApJ, 437, 270
Steffen, M., & Muchmore, D. 1988, A&A, 193, 281
Stencel, R. E. 1987, in Circumstellar Matter, ed. I. Appenzeller (Dordrecht: Reidel), 529
Title, A. M., Shine, R. A., Frank, Z. A., Simon, G. W., & Brandt, P. N. 1995, BAAS, 26, 1464
Uitenbroek, H., & Noyes, R. W. 1994, in Chromospheric Dynamics, ed. M. Carlsson (Oslo: Inst. of Theoretical Astrophysics), 129 (UN)
Uitenbroek, H., Noyes, R. W., & Rabin, D. 1994, ApJ, 432, L67 (UNR)
van Dishoeck, E. F. 1988, in Rate Coefficients in Astrochemistry, ed. T. J. Millar & D. A. Williams (Dordrecht: Kluwer), 49
Vernazza, J. E., Avrett, E. H., & Loeser, R. 1973, ApJ, 184, 605
———. 1981, ApJS, 45, 635
Zirin, H., & Wang, H. 1992, ApJ, 385, L27